Univ.Prof. Friedrich Aumayr

TU WIEN

TECHNISCHE UNIVERSITÄT WIEN

Diplomarbeit

Influence of the Neutral Velocity Distribution on the Results of Pedestal Transport Modeling

Ausgeführt am
Institut für Angewandte Physik
der Technischen Universität Wien
und am
Max-Planck-Institut für Plasmaphysik
in Garching

unter der Anleitung von
Univ.Prof. Dr. Friedrich Aumayr
Univ.Doz. Dr. Elisabeth Wolfrum
durch
Johannes Gnilsen
Matrikelnummer 0926381 Kennzahl 066 461
Gebirgsgasse 88, 1230 Wien

Wien, March 29, 2017   Johannes Gnilsen

Abstract

Particle transport in a plasma plays an important role in fusion research as it determines the dimensioning of a reactor. In the high confinement regime (H-mode) of a tokamak plasma usually repetitive magnetohydrodynamic (MHD) instabilities, so called edge localized modes (ELMs), occur. The H-mode is caused by an edge transport barrier (ETB) in which energy and particle transport is reduced. Due to an ELM event the steep pressure gradients at the edge, that form a pedestal and elevate the profiles in the core region, flatten. The ELM-cycle is closed with the full recovery of the steep edge pressure gradients.

The ELM-cycle is divided into distinct phases corresponding to magnetic modes. Immediately after the ELM crash a *quiet* phase with comparatively low magnetic fluctuations is observed. The onset of mid-frequency fluctuations is followed which determines phase II and is accompanied by an increased particle flux onto the divertor plates. During phase III, characterized by the occurrence of high-frequency fluctuations, the plasma performance reaches pre-ELM behavior again.

Calculations of the density diffusion coefficient D during this ELM cycle were performed using the 1.5 dimensional transport code ASTRA. The impact of a neutral source due to particle recycling at the vessel wall was included with varying neutral energy and density.

Four different assumptions, which were correlated to signals at the divertor and midplane, were considered for the temporal behavior of the particle source.

It was found that the quantification of the diffusion coefficient is not possible without accurate knowledge of the neutral energy and density in each phase of the ELM cycle.

Qualitative results indicate an increased diffusion coefficient after the ELM crash, for all assumptions of the neutral source. For a constant neutral fueling D shows decay-like behavior in phase I until pre-ELM values are reached. This might originate from the reduction of the $\mathbf{E} \times \mathbf{B}$ flow shear in the pedestal after the ELM. Experimentally measured low particle flux in the quiet phase at the divertor is interpreted to originate from reduced density gradients instead of a reduced diffusion coefficient.

In phase II no clear statement is possible without accurate knowledge of the neutral source. It cannot be decided whether the increased particle flux is due

to density gradients ∇n_e only, or also due to an additional increased diffusion coefficient D.

This might lead to the conclusion that MHD modes, visible in the magnetics of the ELM-cycle, are not the modes which dominate particle transport.

Kurzfassung

Der Teilchentransport eines Plasmas spielt für die Fusionsforschung eine wichtige Rolle, da dadurch die Größe eines Fusionsreaktors festgelegt wird. Im Regime hohen Plasmaeinschlusses (H-Mode) eines Tokamak Plasmas treten normalerweise zyklische magnetohydrodynamische Instabilitäten auf, die ELMs genannt werden (Edge Localized Modes). Die H-Mode wird durch eine Randtransportbarriere (ETB) verursacht, wodurch Energie und Teilchentransport am Plasmarand reduziert werden. Durch das Auftreten eines ELM-Events werden die steilen Druckgradienten am Rand, welche das Pedestal bilden und die Plasma Profile erhöhen, flach. Der ELM-Zyklus wird durch die vollständige Wiederherstellung des Randdruckgradienten vollendet.

Der ELM-Zyklus ist in klar unterscheidbare Phasen, erkennbar an den beobachteten magnetischen Moden, eingeteilt. Unmittelbar nach dem ELM-Crash kann die sogenannte *stille* Phase beobachtet werden, in der vergleichsweise wenige magnetische Fluktuationen auftreten. Das Auftreten von mittelfrequenz Fluktuationen charakterisiert Phase II, in der gleichzeitig ein erhöhter Transport auf den Divertor beobachtet wird. Während der Phase III, die durch das Einsetzen von hochfrequenten Fluktuationen bestimmt ist, erreicht das Plasma wieder sein Verhalten vor dem ELM.

Die Berechnung des Dichtediffusionskoeffizienten D wurde während des ELM Zyklus mit dem 1.5 dimensionalen Transportalgorithmus ASTRA durch- geführt. Der Einfluss einer Neutralteilchenquelle aufgrund von Recycling an der Plasmawand wurde berücksichtigt, wobei Energie und Dichte der Quelle varriert wurden.

Vier verschieden Annahmen für die zeitliche Abhängigkeit der Neutralteilchenquelle, bezogen auf Signale am Divertor und an der Midplane, wurden getroffen. Ein Ergebnis der Untersuchng ist die Erkenntnis, dass der Diffusionskoeffizient ohne genaues Wissen der Dichte und Energie der Neutralen nicht quanitifiziert werden kann.

Qualitativ zeigt sich ein erhöhter Diffusionskoeffizient nach dem ELM-Crash für alle Arten der Neutralteilchenquelle. Bei Annahme einer konstanten Quelle zeigt D nach dem ELM ein zerfallsartiges Verhalten bis pre-ELM Werte erreicht werden. Das könnte mit der Reduzierung der $\mathbf{E} \times \mathbf{B}$ Scherströmung im

Pedestal zusammenhängen. Experimentell bestimmte niedrige Teilchenflüsse in der *stillen* Phase treten aufgrund niedriger Dichtegradienten anstelle eines reduzierten Transportkoeffizienten auf.

In Phase II ist keine klare Schlussfolgerung möglich ohne die Neutralteilchenquelle genau zu kennen. Es kann nicht entschieden werden, ob der erhöhte Teilchentransport in dieser Phase nur von erhöhten Dichtegradienten resultiert oder auch von einer zusätzliche Erhöhung des Transportkoeffizienten.

Eine allgemeine, vorsichtige Schlussfolgerung könnte jedoch sein, dass der Teilchentransport nicht von den MHD Moden, die in der Magnetsignatur des ELM Zyklus beobachtet werden können, verursacht wird.

Contents

1. Motivation

1.1. Need for Fusion Energy

The exploitation of fossil fuels like coal or oil brought incredible prosperity to industrialized states [1]. For the greatest part of human history muscular strength was the only way to do most kinds of work. Invention of different machines in the 19th century that combust fuel took over to perform the most exhausting tasks. This ease severely changed human living and further invention of technologies evolved human society. Nowadays, human energy consumption is much higher compared to the pre-industrial era. Industrialization of developing countries like China or India leads to additional growth of global energy consumption.

But combustion of fuels releases greenhouse gases that slowly warm up the atmosphere and causes disastrous effects on natural equilibrium. Oil, which is one of the most important energy sources due to its high combustible energy density, cannot be found everywhere on earth. Wars and involvement into political intrigues are therefore often consequences for oil exporting countries [1]. Awareness of these issues and the fact of limited availability of fossil fuels let governments search for alternative sources of energy. Solar power and wind power are accessible everywhere on earth but are not sufficient to supply the basic load of the electric grid.

In the 20th century physicists revealed the enormous potential of power that is stored in the binding energy of atoms. The energy density of nuclear fuel is several million times bigger than the energy density of combustibles. During World War II the concept for a nuclear power plant was evolved, in which heavy U_{235} isotopes fissile to lighter nuclei, thereby releasing high amounts of energy. Today, nuclear power provides more than only few parts of the total electricity produced and nuclear power plants can be seen as important suppliers in different countries. As this kind of energy production is based on controlling a chain reaction, failure can be fatal and lead to nuclear disasters.

Fusion of two light nuclei to a heavier one is based on the same physical background but has to be achieved in a completely different way. Developing a reactor that can exploit this fascinating source of energy is the current aim of research. Unlike in the case of fissile power plants there would be no long term radioactive waste and no need to control a chain reaction. The fuel is also available nearly everywhere on earth and cheap. Only the realization of a fusion power plant turned out to be very tricky, expensive and has not been achieved yet. On the other hand, clean energy supply could be guaranteed by working fusion reactors which could totally reward these investments.

1.2. Controlled Fusion Background

In principle fusion reactions occur in case of two (or more) nuclei getting close enough to each other to get into the influence of the attractive, but very short ranged, strong interaction force which is responsible to form nuclei. As the nuclei are both positively charged, they are repelled by each other due to the long ranged Coulomb force. One solution to overcome this repulsive Coulomb force is given by the sun. It confines particles under their own gravitational field and compresses the nuclei close enough to each other to fuse them. Generation of such high pressures is not possible on earth.

An idea is to heat a gas of fusion reaction partners to increase their kinetic energy. If two nuclei then collide and their kinetic energy is high enough to overcome the Coulomb barrier, a desired fusion reaction can occur. In this case quantum mechanics play a significant role, as it allows particles to tunnel the upper part of the Coulomb barrier which reduces the required temperature significantly. Still, the temperature of this gas has to be in the order of 10 keV which corresponds to $100 \cdot 10^6$ K in SI units. Because any contact of this very hot gas with solid or liquid surfaces would immediately absorb a crucial amount of its energy preventing fusion reactions to happen, a confinement system without contacting surfaces has to be worked out.

Components of a neutral gas lose several or all their electrons at high temperatures, which leads to a gas consisting of charged particles, the so called plasma state.

Charged particles are generally interacting with magnetic and electric fields and the Lorentz Force $\mathbf{F}_L = q(\mathbf{E} + \mathbf{v} \times \mathbf{B})$ lets charged particles gyrate around mag-

netic field lines with the Larmor radius r_{L}. Up to a certain point perpendicular transport can be suppressed this way. The concept which exploits this effect to confine the plasma particles without contacting wall surfaces is called magnetic confinement. The tokamak, which will be described later in section 1.3, is the currently best performing realization of a magnetic confinement device.

The cross section for a fusion reaction is smaller than the cross section for a Coulomb collision. Therefore several collisions are required to finally fuse two nuclei. In figure 1.1 the rate coefficients for different fusion reactions are shown. The fusion cross section of the two hydrogen isotopes deuterium (D) and tritium (T) was found to be the biggest for a given temperature compared to all other fusion reactions. Hence, the first nuclear fusion power plants will be designed to work with a D-T plasma, although the clean D-D (no usage of radioactive tritium) and D-He$_3$ (all fusion products are charged and therefore confined) reaction would be more favorable.

Deuterium can be found in one out of 6700 hydrogen atoms in H_2O and therefore easily gained from the ocean. Sufficient tritium supply is due to its short half-life a major issue in fusion research, but the common idea is to breed it from a lithium blanket that surrounds the vessel wall of a fusion reactor.
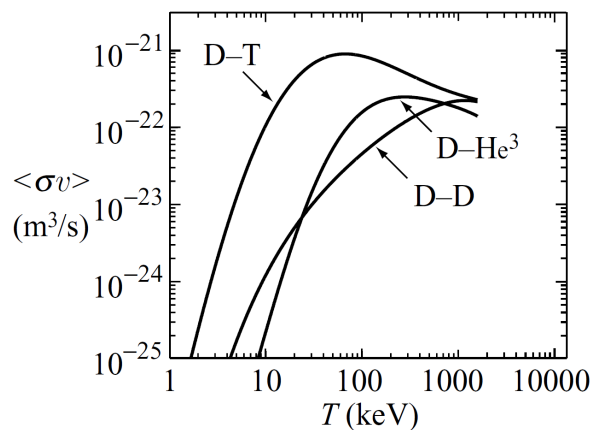

Figure 1.1.: Rate coefficients from different fusion reactions. The temperature is given in units of keV. Conversion with Boltzmann's constant k_{B} gives 1 eV = 11 600 K. Figure taken from [2].

As it is shown in equation 1.1 the D-T fusion reaction yields an uncharged neutron, a positively charged α-particle (nucleus of He_4^2) and 17.6 MeV kinetic

3

energy of the fusion products. Responsible for this energy gain is the well known mass defect, described by the formula $E = \Delta mc^2$.

$$D_2^1 + T_3^1 \rightarrow n_0 + He_4^2 + 17.6\text{MeV} \tag{1.1}$$

While the positively charged α-particle remains in the confined plasma region the neutron escapes from it and collides with the vessel wall. Thereby its kinetic energy is converted to heat in the wall components which will further be transformed into electrical energy by heat exchangers and steam generators. Due to collisions of the remaining α with the plasma particles the plasma will be intrinsically heated. If the fusion rate is high enough, all energy losses can be balanced in this way and the required plasma temperature can be maintained without external power supply - the plasma ignites.

The limit to achieve ignition is described by the Lawson Criterion [3] which gives a threshold for macroscopic plasma parameters. It can be expressed by the triple product of temperature T, density n and energy confinement time τ_E

$$nT\tau_E \geq 3 \times 10^{21}\text{m}^{-3}\text{keV s}. \tag{1.2}$$

The factor on the right hand side of equation 1.2 depends on the temperature and density profiles or impurities [3]. It generally does not matter how this fusion product is achieved and there are different plans to get there. In contrast to the concept of magnetic confinement, which is based on a comparatively long energy confinement time at low densities, the idea of inertial confinement suggests to compress fusion fuel with pulsed laser shots to very high densities at very short τ_E (see table 1.1). This completely different approach is mentioned here for the sake of completeness and won't be further discussed. Typical plasma values for these two approaches are shown in table 1.1.

Approach	n [m^{-3}]	T [keV]	τ_E [s]
magnetic confinement	10^{20}	10	10
inertial confinement	10^{31}	10	10^{-11}

Table 1.1.: Typical values for different approaches to achieve the Lawson Criterion.

The next section deals with the difficulty to confine a hot plasma for a sufficiently long period of time and introduces the tokamak concept.

1.3. The Tokamak Principle

One of the main obstacles in early fusion devices in the 1950s was the occurrence of evolving instabilities under plasma operation [4]. Investigation of several possible configurations like pinches or mirror machines didn't qualify them for the demands of magnetic confinement fusion. Pinches are highly unstable and different kinds of disturbances lead to a collapse of the plasma column [5]. Magnetic mirrors fail at particle confinement due to an unavoidable fraction of plasma losses.

In 1968 electron temperatures above 2 keV for significantly long times could be measured in a so-called tokamak device [6]. These surprisingly good early results led subsequent research to mainly concentrate on the tokamak principle as it seemed promising for the realization of a fusion power plant.

The characterizing feature of a tokamak is a toroidally shaped plasma column and the comparatively simple two dimensional coil configuration. A sketch of such a device is shown in figure 1.2. Due to its closed geometry particle losses along the magnetic field lines can be avoided. The toroidal field is produced by planar D-shaped coils. A superimposed poloidal field component stabilizes the plasma column.

The major radius of the torus is denoted by R_0 and the minor radius by a. For a medium sized tokamak like ASDEX Upgrade (axial symmetric divertor experiment) these quantities are 1.65 m and 0.5 m, respectively.

The picture of gyrating particles around field lines given before (see section 1.2) is only applicable for straight field lines. As soon as the plasma is bent curvature drifts in perpendicular direction appear. Transverse gradients of the magnetic field ($\mathbf{B}(\mathbf{r}) \propto \frac{1}{r}$) are the origin of the so called ∇B drift. If no currents are present, the ∇B drift and curvature drift point in the same direction and the corresponding equations have similar form. These drifts can then be combined to

$$\mathbf{v}_d = \frac{v_\parallel^2 + \frac{1}{2}v_\perp}{\omega_\mathrm{C}} \frac{\mathbf{B} \times \nabla B}{B^2} \tag{1.3}$$

in which the parallel and perpendicular component originate from curvature and ∇B drift, respectively. The cyclotron frequency ω_C is charge dependent and inversely proportional to the magnetic field B.

This drift separates ions and electrons producing an electric field which causes a further prominent drift. The $\mathbf{E} \times \mathbf{B}$ drift results from perpendicular magnetic and electric fields. Because of its charge independence it pushes both species of plasma components out of the confined region with a velocity denoted in equation 1.4.

$$\mathbf{v}_{d,E \times B} = \frac{\mathbf{E} \times \mathbf{B}}{B^2} \tag{1.4}$$

An additional example of particle motions is the polarization drift as a consequence of a time dependent electric field [3].
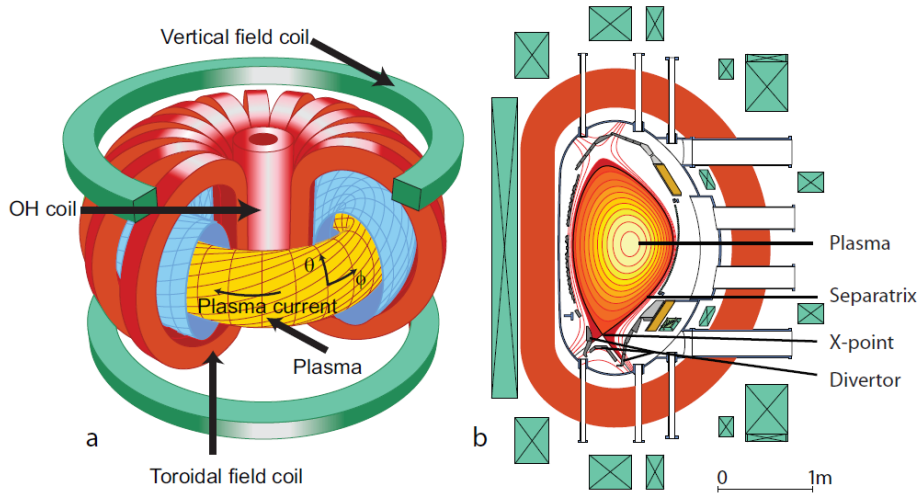

Figure 1.2.: Schematic (a) and poloidal (b) cross section of the tokamak principle. It can be seen that the shape of the plasma column is elongated, as this returns better plasma performance. Figure taken from [7].

To improve particle confinement a central solenoid which acts as an ohmic transformer is implemented into the machine. Thereby a plasma current I_p can be induced with a corresponding magnetic field. Composition of all magnetic fields give a helical field line trajectory, on which particles can follow and stay in the confined plasma for a longer period of time. The safety factor q describes the average twist of the magnetic field lines on a flux surface [3]. On the other hand this configuration gives rise to a weakness of the tokamak principle, as it

can only be operated in pulse-like shots. Additional ideas for steady state power plant operation have to be worked out.

Modern machines like *JT-60SA* in Japan or the next-step device *ITER* will be equipped with supraconducting coils. This extends the duration of a plasma discharge as the necessary current can be applied for a longer time without overheating the components. In addition to the difficulties for engineers to implement supraconducting coils, the appearing electromagnetic forces point in different directions and are very large. A supporting structure is required in order to prevent the device from structural disintegration.

Continuous neutron bombardment, as it will be the case in a nuclear power plant, still challenges material scientists to get applicable wall components. Thereby activated vessel elements cause some radioactivity. These components have to be stored (or reprocessed) for ~ 100 years until their radioactive emission can't be distinguished from natural radiation.

The divertor, which is drawn in figure 1.2b, is also a feature of various tokamak machines. It forms the last closed flux surface (LCFS or also often called separatrix) to have an X-point which divides the plasma into the scrape-off layer (SOL) and the confined region. The particles of the SOL are directed onto the divertor targets which are made of specially designed plates, that can be exposed to high heat loads.

In comparison to the tokamak principle the stellerator design can turn out to be another concept for a future power plant. The currently biggest stellerator experiment *Wendelstein 7-X*, which started operation in December 2015 in Greifswald, Germany shall give an answer to this question.

1.4. High Confinement Mode Phenomena

In 1982 the high confinement regime (H-mode) was discovered at the ASDEX tokamak. Beyond a certain threshold of neutral beam injection (NBI) heating power the H_α and D_α signals at the divertor decreased suddenly [8]. Increased particle confinement was also observed and further an increased energy confinement time τ_E by a factor of two [9]. H-mode operation does not depend on the method of auxiliary heating and can also be achieved without divertor configuration (limiter operation) [10].

Future fusion devices like ITER will be operated in this regime. In comparison

to the low confinement mode (L-mode) steep pressure ($p = nT$) gradients are localized at the plasma edge. This is shown in figure 1.3. An evolving edge transport barrier (ETB), which can be seen as a narrow region with reduced particle and heat transport at the plasma edge, was found to be responsible for this improvement. It forms a pedestal which elevates the pressure profile and increases therefore the whole plasma performance.
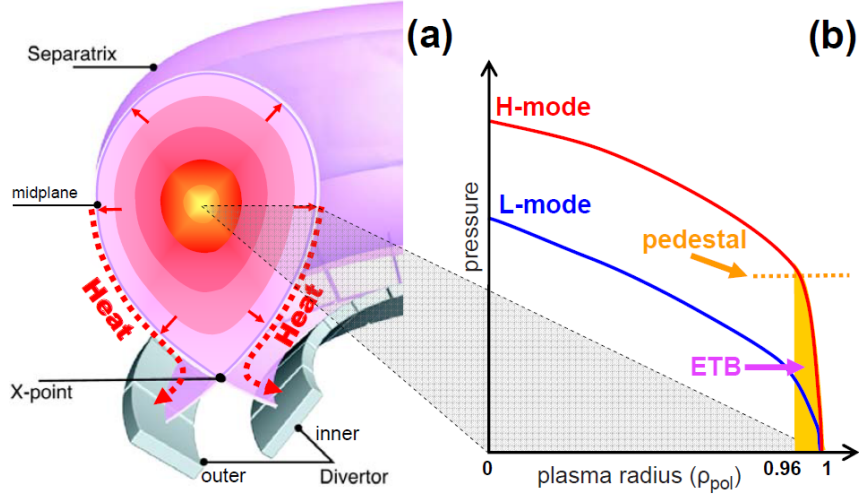

Figure 1.3.: Plasma in divertor configuration (a) and pressure profiles of H- and L-mode (b). Picture taken from [12].

H-mode operation is normally accompanied by quasi-periodic magnetohydrodynamic (MHD) instabilities that release particles and energy into the SOL in a very short time interval (< 1 ms). These events are known as edge localized modes (ELMs). Reducing the confined energy by about 10-20% they impose a huge heat load on plasma facing components, which can be critical for larger machines like ITER. On the other hand a beneficial effect is the flushing of impurities, which would accumulate during the discharge and emit energy via radiation. Understanding of the triggering mechanisms are desirable and although ELMs are not fully understood yet, various studies are already existing [11]. During this burst like ejection the steep edge pressure gradients flatten and the pedestal collapses. In the following recovery phase the temperature and density gradients rebuild on different time scales until the pedestal is completely restored and the next ELM event occurs [12, 14]. In this work the pedestal

recovery process is investigated with particular regards to the behaviour of the diffusion coefficient and the influence of neutral particles on it.

1.5. Objectives of this Thesis

Aim of this work is the investigation of the diffusion transport coefficient in the pedestal region of a tokamak plasma. Based on different assumptions the diffusion coefficient shall be quantified in different phases of the pedestal recovery after an ELM crash. The calculations are performed for a *representative ELM cycle* obtained from *ELM synchronization*. This method is explained later in section 3.3.

Chapter 2 introduces general aspects of transport in a plasma to describe the physical background on which this thesis is based. Three different transport regimes *classical*, *neoclassical* and *turbulent* transport are shortly described. The diffusion equation is derived qualitatively and the role of neutrals coming from the vessel wall is highlighted.

Plasma particles that hit the wall are generally reflected as neutral atoms or molecules with a certain energy distribution. As soon as they are ionized they follow the magnetic field lines. There is a certain possibility that neutrals cross the SOL and get into the confined region, where they act as a plasma source. Calculations in this work shall take this issue into account and the neutral source shall be modeled considering several assumptions.

Different cases of the temporal behavior of neutrals during the ELM cycle are investigated. Energy and density of these neutrals are varied. The energy variation is related to energetic neutrals produced in the scrape-off layer by Franck-Condon processes or by reflection from the metal wall.

The total diffusion coefficient obtained from simulations for different ELM cycle phases shall be compared to previously found results [17, 18]. Computations are performed with the ASTRA code and the neutral source is estimated by the KN1D code. These codes will be explained in an extra chapter to show their assumptions and boundary conditions.

The results are described and shown in several simulations. In a final discussion the results of this work are interpreted and suggestions for future investigations of the diffusion coefficient are made.

2. Transport in a Tokamak Plasma

Transport in plasmas is a very important subject as it determines the dimensioning of fusion devices. Investigation of transport coefficients and the understanding of their mechanisms are therefore essential for fusion research. In history different transport regimes have been found and described as experimental data didn't match with classical theoretical predictions. The measured quantities were orders of magnitudes higher than first assumed. Various mechanisms are responsible for higher transport which requires in general to operate with bigger plasma volumes to get a sufficiently high energy confinement.

In this work the diffusion coefficient of the pedestal region is investigated in which the pedestal is assumed to be mainly diffusive [17].

The next section gives a short overview of different transport regimes and the mathematical background to derive the diffusion equation is explained afterwards. The consideration of neutrals is explained in the last section of this chapter.

2.1. Transport Regimes

A common way to describe the phenomenon of diffusion in a mathematical framework is the concept of the *Random Walk*. Thereby particles move each time interval Δt randomly in any arbitrary direction $(\pm \Delta x, \pm \Delta y, \pm \Delta z)$, while the absolute value of the step size doesn't change. After further calculations one can derive an expression for the particle flux in any direction, which is also known as *Fick's law* (equation 2.1) and plays an important role to derive the diffusion equation.

$$\mathbf{\Gamma} = -D\nabla n \tag{2.1}$$

In equation 2.1 the flux $\boldsymbol{\Gamma}$ is described as balancing result of a density gradient ∇n times a coefficient D, which is called diffusion coefficient.

Classical Transport is based on Coulomb collisions of the charged plasma components. The time between collisions is assumed as $\Delta t = 1/\nu$, in which ν stands for the collision frequency. The average displacement due to collisions corresponds to the gyration radius r_{L} and the diffusion coefficient for classical diffusion can be derived as

$$D_{class} = r_{\mathrm{L}}^2 \nu \tag{2.2}$$

The same result can be obtained in the fluid picture of a plasma which combines fluid equations with Maxwell equations and is called magnetohydrodynamics (MHD) [19].

It has to be mentioned here that only collisions with unlike particles contribute to a net diffusion. Identical ions or electrons exchanging their momentum can be seen as transposition of each other. On the contrary energy transport is carried out also for like particles.

Ions and electrons diffuse in general with different velocities due to their unequal mass. Charge separation leads to an electric field that acts as a counter force for the much faster diffusing electrons. This is known as *ambipolar diffusion* which combines the two distinct diffusion coefficients to the same for both plasma species.

As it turned out, theoretical results of classical diffusion are not found experimentally. For typical plasma parameters the diffusion coefficient is calculated this way to be in the range of $D \sim 10^{-5} - 10^{-4}$ m^{2}s^{-1}. Indeed experimental data reveal the value for D to be near 0.1 m^{2}s^{-1} in the pedestal region [18, 19] and D ~ 1 m^{2}s^{-1} in the core.

Neoclassical Transport describes transport which is caused by trapped particles. In the toroidal geometry of a tokamak field the magnetic field is higher at the center (high field side HFS) than outside (low field side LFS). The magnitude of $\mathbf{B}$ follows a law like $\mathbf{B}(\mathrm{r}) \propto 1/r$.

Therefore particles are trapped in what seems to be similar to magnetic mirrors on so called banana orbits. Consequently the step size due to a collision is the bananawidth ω_{B} which is significantly larger than the radius of gyration r_{L}. An effective collision frequency ν_{eff} is connected to the time a particle stays in a

trapped orbit until it gets enough parallel energy to leave it.

Including the bananawidth ω_{B}, the fraction of trapped particles n_{TR}/n in banana orbits and ν_{eff} the neoclassical diffusion coefficient can be estimated to be [19]

$$D_{\mathrm{neo}} = \omega_{\mathrm{B}}\nu_{\mathrm{eff}}\frac{n_{\mathrm{TR}}}{n} \approx \frac{q^2}{\epsilon^{3/2}}D_{\mathrm{class}} \qquad (2.3)$$

In equation 2.3 ϵ denotes the inverse aspect-ratio $\epsilon = (R_0/a)^{-1}$ and q is the safety factor. The diffusion coefficient obtained for neoclassical transport is about two orders of magnitude larger than that for classical transport but still too small to fit experimental measurements. These phenomena can be deduced from the toroidal geometry of the tokamak device.

Another important quantity to characterize a plasma is the collisionality ν^* which can be described as product of the time a particle needs to fulfill a banana gyration Δt and the effective collision frequency ν_{eff} (equation 2.4).

$$\nu^* = \nu_{\mathrm{eff}}\Delta t \qquad (2.4)$$

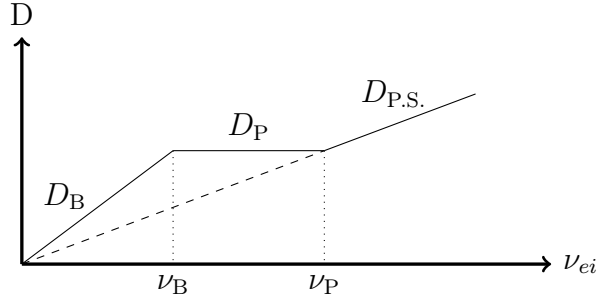

Figure 2.1.: Neoclassical diffusion coefficient D [m²s⁻¹] as function of collisionality. The diffusion coefficient for the banana regime D_{B}, the plateau regime D_{P} and the Pfirsch-Schlüter $D_{\mathrm{P.S.}}$ regime are shown. The frequency to complete a banana orbit is given by ν_{B} and ν_{p} gives the frequency from which MHD is applicable [9].

Figure 2.1 shows three different neoclassical regimes for particle transport that can be characterized as function of the collisionality of a plasma. The plasma discharge investigated in this work exhibits a high collisionality ($\nu^* > 1$) and the neoclassical diffusion coefficient can therefore be found in the Pfirsch-Schlüter

regime [3].

Turbulent Transport can be described in the kinetic picture of the plasma. It turned out that binary collisions cannot be the only reason for the observed plasma behavior. Fluctuations are often assumed to be responsible for high radial transport. In general fluctuations are driven by pressure gradients perpendicular to the magnetic field [4].

Typical spatial dimensions of such fluctuations are in the cm range. If these turbulent structures last about 10^{-4} s a diffusion coefficient in the random walk model can be estimated to D ≈ 1 m^{2}s^{-1}. Fluctuations are especially observed at the edge of a tokamak plasma. An analytical description of this behavior is not possible in most cases and numerical methods have to be applied [19].

For completeness it is mentioned here that the energy transport can be described with similar considerations as mentioned before. In this work the pedestal is assumed to be mainly diffusive and the particle flux can be described by Fick's law, equation 2.1.

2.2. Diffusion Equation

In order to derive an equation for the particle transport all particle sources and sinks in a certain volume have to be balanced. The rate of change for particles is given by the difference of produced particles in a volume and number of particles leaving the surface of this volume. Equation 2.5 describes this situation.

$$\frac{\partial N}{\partial t} = - \oint_{\partial V} \mathbf{\Gamma} d\mathbf{A} + \int_V S dV \tag{2.5}$$

The density, generally described by $n(\mathbf{r}, t) = dN/dV$ and the usage of Gauss law ($\oint \mathbf{\Gamma} d\mathbf{A} = \int \nabla \cdot \mathbf{\Gamma} dV$) yields the continuity equation.

The continuity equation can now be written as

$$\frac{\partial}{\partial t} n(\mathbf{r}, t) = -\nabla \cdot \mathbf{\Gamma}(\mathbf{r}, t) + S(\mathbf{r}, t) \tag{2.6}$$

In equations 2.6 and 2.5 the flux of the diffusive material is described by $\mathbf{\Gamma}$. It is

composed of two assumptions which are shown in equation 2.7.

$$\mathbf{\Gamma}(\mathbf{r}, t) = -D(\mathbf{r}, t)\nabla n(\mathbf{r}, t) + n(\mathbf{r}, t)\mathbf{v}(\mathbf{r}, t) \tag{2.7}$$

The first term on the right hand side is known as Fick's first law (*diffusion approximation*, see section 2.1) and describes the flux as balancing act of a density gradient. The second term gives a flux due to a particle drift and is neglected in the further derivation. Combination of equation 2.7 with the continuity equation yields the diffusion equation which is denoted as

$$\frac{\partial}{\partial t} n(\mathbf{r}, t) = \nabla \cdot [D(\mathbf{r}, t)\nabla n(\mathbf{r}, t)] + S(\mathbf{r}, t) \tag{2.8}$$

In this case and in general the diffusion coefficient $D(\mathbf{r}, t)$ is not constant. In case of an anisotropic flux the diffusion coefficient has also to be considered as tensor and equation 2.8 becomes non linear for a density dependent D.

In further calculations a spatially constant diffusion coefficient is assumed and equation 2.8 reduces to the following differential equation

$$\frac{\partial}{\partial t} n(\mathbf{r}, t) - D\nabla^2 n(\mathbf{r}, t) = S(\mathbf{r}, t) \tag{2.9}$$

The equation is generic in terms of geometry and has to be transformed to toroidal coordinates for a tokamak system.

Equation 2.9 is shown again in cylindrical coordinates for an isotropic density $n(r, \theta, z, t) = n(r, t)$. The term that shows the $1/r$ dependence also appears in toroidal coordinates and is important if a tokamak configuration is considered.

$$\frac{\partial}{\partial t} n(r, t) - D\left[\frac{1}{r}\frac{\partial n(r, t)}{\partial r} + \frac{\partial^2 n(r, t)}{\partial r^2}\right] = S(r, t) \tag{2.10}$$

Estimations for the particle confinement can be performed with the ansatz $n(\mathbf{r}, t) = n(\mathbf{r})\exp(-t/\tau_p)$ which links the diffusion coefficient directly to the particle confinement time τ_p (neglecting the source term).

$$\nabla \cdot [D\nabla n(\mathbf{r})] = -\frac{1}{\tau_p} n(\mathbf{r}) \tag{2.11}$$

In the following chapter the plasma source $S(\mathbf{r}, t)$ which is assumed to originate from ionized neutral particles will be described.

14

2.3. The Role of Neutral Particles in the Pedestal

In equation 2.9 an external plasma source is included on the right hand side. In this section the origin of this source is discussed.

When an expelled ion hit the vessel wall it can be reflected as energetic neutral, bound on the surface and released as thermal atom or molecule or diffuse deeper in the material and is stored. After some delay it can be released as thermal particles.

The return of particles into the confined plasma due to these processes is called recycling. The new born neutrals move towards the confined region through the scrape-off layer and collide with particles. Due to these collisions the neutrals can be excited or ionized. If the ionization process is located inside the separatrix the former neutral stays confined and is added to the plasma.

The reflection coefficient at the wall and the corresponding velocity is dependent on the materials at which the ions get recycled. The special feature of tungsten covered tiles in ASDEX Upgrade plays an important role, as it affects the energy of recycled atoms and molecules [20]. Because of the higher atomic number of tungsten (Z_W=74) in comparison to carbon (Z_C=6), which is also a common first wall material, the mass ratio of collision partners in the W case is obviously different than in the C case. Therefore, less momentum is transmitted which lowers the ion moderation. As it can be seen in the formula for the *Rutherford cross section* (equation 2.12) higher Z leads to an increased collision probability [4].

$$\frac{\mathrm{d}\sigma}{\mathrm{d}\Omega} = \left(\frac{1}{4\pi\epsilon_0} \frac{Z_1 Z_2 e^2}{4 E_0} \right)^2 \frac{1}{\sin^4\left(\frac{\theta}{2}\right)} \tag{2.12}$$

A comparison for different impacting energies E_0 of deuterium onto different wall material is shown in table 2.1.

	D → C			D → W		
E_0	R_P	R_E	$\langle E \rangle$	R_P	R_E	$\langle E \rangle$
10 eV	0.40	0.13	3.5 eV	0.80	0.60	7.5 eV
20 eV	0.32	0.12	7.5 eV	0.71	0.52	14.6 eV
50 eV	0.30	0.10	16.6 eV	0.68	0.38	27.9 eV

Table 2.1.: Values of particle reflection coefficient R_P and energy reflection coefficient R_E for incident deuterium with energy E_0. The mean reflection energy $\langle E \rangle$ is calculated for carbon (C) and tungsten (W) covered tiles [20].

The ionization of neutrals from the wall to the separatrix is dependent on the electron density n_e and temperature T_e in the SOL. Modeling the scrape-off layer is therefore necessary to get reliable results for the ionization rates. Simulations at ASDEX Upgrade revealed higher densities for neutrals with characteristic energies that cross the separatrix. They might result from Franck-Condon dissociation processes that can create an energetic neutral from molecular hydrogen as it is shown in the list below [15].

a) $H_2 + e^- \rightarrow H + H^*$ (3.0 eV)

b) $H_2 + e^- \rightarrow H + H^+$ (5.0 eV)
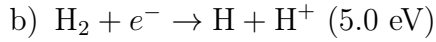
The two dimensional spatial density distributions for neutral deuterium atoms, molecules and electrons, calculated from EMC3-EIRENE simulations [20], are shown in figure 2.2. The electron density is high within the separatrix and at the divertor.

The value of the neutral density is high at the divertor and outer midplane compared to the other SOL regions. The absolute atomic neutral density is about 10^{16} m^{-3} at the separatrix.
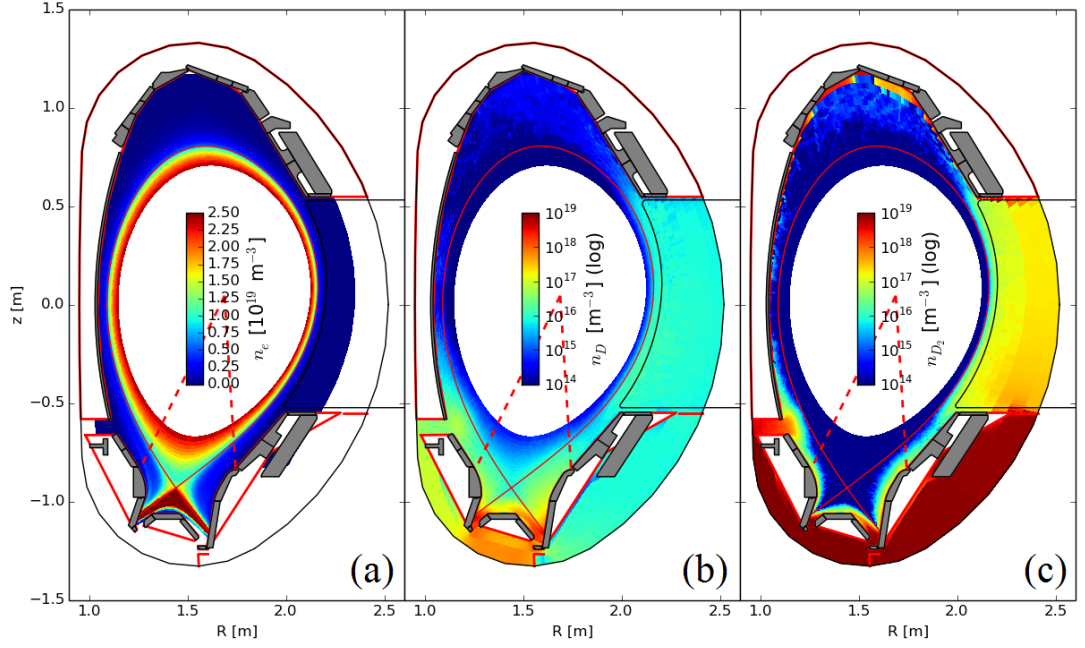
Figure 2.2.: Poloidal cross section for simulated electron density (a), atomic (b) and molecular neutral (c) density. The distribution is obtained from calculations with the EMC3-EIRENE code. Figure taken from [20].

It is discussed later that one dimensional temperature and density profiles serve as input for the ASTRA code. The two dimensional geometry of the spatial neutral density distribution has to be reduced to a one dimensional value given at the separatrix at the midplane. Because no two dimensional calculations of scrape-off layer physics are performed in this work, different cases for neutral behavior at the separatrix are modeled and investigated. These are described in detail in chapter 4.

3. Experiment

To investigate the inter-ELM profile recovery in the pedestal experiments are performed. The profile evaluation has been performed by Laggner [12] and Keerl [13]. A fast electron density increase after the ELM crash is observed in all investigated discharges. In this chapter the diagnostics for the edge profiles and the method of ELM synchronization are described. Density and temperature profiles are a necessary input for the modeling.

The density and temperature profiles are split into distinct phases according to the magnetic characteristic which are observed during the ELM cycle in the experiment. These phases are introduced in this chapter and kept for the whole work.

3.1. Diagnostics

3.1.1. Lithium Beam

The Lithium-Beam (LiB) diagnostic is a tool to determine the plasma density at the plasma edge. It is based on the observation of $Li(2p) \rightarrow Li(2s)$ transition that emits a photon with wavelength $\lambda = 670.8$ nm. Measurement of the intensity of this transition $I_{Li(2p \rightarrow 2s)}$ yields information about the electron density.

Li ions are emitted at the emitter, accelerated to 30-60 keV, focussed and neutralized in a sodium (Na) charge exchange cell. The spatial line emission profiles are modeled including impact excitation, ionization and charge exchange processes. The occupation density N_i for the i-th excited state of lithium along the z-axis is given by

$$\frac{dN_i(z)}{dz} = \sum_{j=0}^{9}[n_e(z)a_{ij}(T_e(z)) + b_{ij}]N_j(z) \tag{3.1}$$

in which a_{ij} denotes the coefficients for excitation and de-excitation and b_{ij} the coefficients for spontaneous emission. Density and temperature profiles are de-

noted by n_e and T_e, respectively.

At the plasma edge all Li-atoms are assumed to be in the ground state

$$N_i(z = 0) = \delta_{1i} \tag{3.2}$$

This coupled linear differential initial problem (equation 3.1 and 3.2) is solved using Bayesian probability theory [21].

The emitted photons are detected with two optical systems. The beam has a diameter of 10-15 mm. To allow background subtraction the beam is chopped [22]. Radial solution for the density profiles of about 5 mm can be achieved.

3.1.2. Electron Cyclotron Emission

With the electron cyclotron emission spectroscopy temperature profiles of the plasma can be measured.

In a magnetic field electrons gyrate around the field lines with a certain frequency ω_C according to

$$\omega_C = \frac{eB}{m_e} \tag{3.3}$$

The electron charge is e, B the magnetic field and m_e the electron mass. The radial dependence of $B(r) \propto 1/r$ in a tokamak plasma leads therefore to a radial dependency of the cyclotron frequency ω_C. This issue is exploited to control the location of power deposition in the core of the plasma by cyclotron heating. Measuring the frequency of the emitted radiation, a profile of the temperature can be determined using only one line of sight.

Nowadays fusion plasmas are mostly optically thick and radiation of all frequencies is absorbed by cyclotron resonances. A black body at a certain temperature T, that absorbs all radiation, described in *Kirchhoff's law of thermal radiation*, also emits radiation with a spectral distribution $I(\nu)$ described in *Planck's law* (equation 3.4).

$$I(\nu) = \frac{8\pi h \nu^3}{c^3} \frac{1}{e^{h\nu/k_B T} - 1} \tag{3.4}$$

The frequency ν can also be expressed by the angular frequency $\nu = \omega/2\pi$. In equation 3.4 the speed of light is denoted by c, Planck's constant is given by h and Boltzmann's constant is written as k_B. Today fusion plasmas have $h\nu \ll k_B T$ which allows an approximation $e^{h\nu/k_B T} \approx 1 + h\nu/k_B T$ and equation 3.4 can be

approximated to the law of *Rayleigh-Jeans*

$$I(\nu) \approx \frac{8\pi}{c^3} \nu^2 k_{\mathrm{B}} T \qquad (3.5)$$

Combining equations 3.3 and 3.5, measurement of $I(\nu)$ gives the electron temperature profile if $\omega_{\mathrm{C}}(r)$ is known.

$$T_e(I(\nu), \omega_{\mathrm{C}}(r)) = \frac{4\pi^2 c^3}{k_{\mathrm{B}}} \frac{I(\nu)}{\omega_{\mathrm{C}}(r)^2} \qquad (3.6)$$

In the SOL the optical thickness of the plasma quickly drops and no reliable measurements are therefore possible.

3.1.3. Integrated Data Analysis

In conventional data analysis the measured quantities of each diagnostic are analyzed and mapped separately onto a coordinate system. Afterwards the results are combined.

Problems can occur if the data of different diagnostics is partially non consistent and the validation of the data subset relies on the expertise and judgement of the analyzing person. This non standardized approach leads to difficulties comparing results of internationally obtained results [21] and diagnostic specific issues might be lost.

The integrated data analysis (IDA) combines raw data of complementary diagnostics and n_e and T_e profiles, which fit best to the data and their uncertainties are derived within the framework of Bayesian probability theory. Thereby joint density and temperature profiles are obtained.

Profiles of ECE, LiB, deuterium cyanide laser interferometry (DCN) and Thomson scattering (TS) are analyzed in the IDA approach. The combination of the LiB spectroscopy and the DCN interferometry lead to a density profile that reaches from the core to the separatrix, especially accurate at the plasma edge due to the high reliability of the LiB diagnostic. The correct interpretation of ECE signals depends on the density profile n_e which can now be acquired from the combining IDA approach. Thomson scattering is the only diagnostic that can simultaneously measure T_e and n_e profiles and therefore provides an important link between these two quantities. The alignment of the different profiles can therefore be obtained from comparison with TS.

3.2. Shot #30701 Parameters

Discharge No. 30701 is investigated in this thesis. Because of low ELM frequencies of about 70 Hz the pedestal recovery phase is long and can be well analyzed [12]. The plasma was operated in lower single null (LSN) mode. Global discharge parameters are plasma current I_p = 1 MA and toroidal field B_T = -2.5 T. The negative sign indicates the opposite direction of the current I_p. The plasma was heated by neutral beam injection (NBI) of 4.3 MW and electron cyclotron resonance heating (ECRH) of 0.7 MW.

The time window of interest of this shot is from 2.975 s to 3.4 s in which the plasma parameters stay constant and ELMs with similar size occur at constant frequency. This allows a statistic investigation of ELM events.

An overview plot of #30701 2.975s - 3.4 s is given in figure 3.1. The evolution of the temperature and density profiles is shown as well as the injected power by the electron cyclotron resonance heating (ECRH) and neutral beam injection (NBI). The signal of the density and temperature profiles are repetitively interrupted due to the chopping of the lithium beam and the further processing with IDA. In general the profiles as well as the ELM frequency are sufficiently constant to allow statistical analysis by ELM synchronization.

The divertor shunt current I is shown in the fourth panel of figure 3.1. From the rising flank of the signal the time of each ELM onset can be determined.
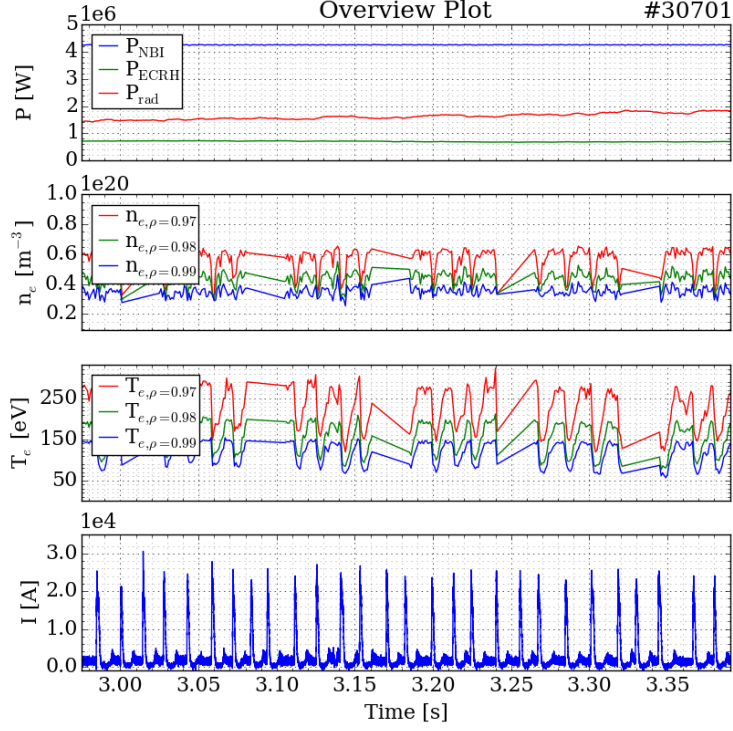
Figure 3.1.: Time trace of shot #30701 for 2.975 s to 3.4 s. Panel 1: time trace of the input power. P_{NBI} (blue) and P_{ECRH} (green) as well as radiated power P_{rad} (red). Panel 2: electron density at three different radial positions, $\rho = 0.97$ (red), $\rho = 0.98$ (green) and $\rho = 0.99$ (blue). Panel 3: electron temperature T_e, the same color code is used for the density. Panel 4: current measured in the divertor to determine the time of each ELM onset.

3.3. The ELM Cycle

The method of ELM synchronization is based on the the quasi-periodic appearance of ELMs. The behavior of the pedestal recovery after an ELM crash is similar in each ELM cycle and the method is used to obtain better, statistically reliable data. Thereby, the ELM onset time $t_{ELM} = 0$ is determined for each ELM from the rising flank of the divertor shunt current measurements. The signal, that is ELM-synchronized, is divided into time-spans around each ELM, and the new time-base locked to $t_{ELM} = 0$ is applied. This procedure allows the averaging of signals in time windows relative to the time of ELM onset.

The ELM synchronization is performed to obtain a single representative ELM

cycle within the time window from 2.975 s to 3.4 s of the discharge #30701. In this thesis in general all data is ELM synchronized before used in the simulations. In figure 3.2 the ELM synchronized magnetic behavior of this discharge is shown. The ELM cycle can be divided into distinct phases corresponding to the magnetic fluctuations.
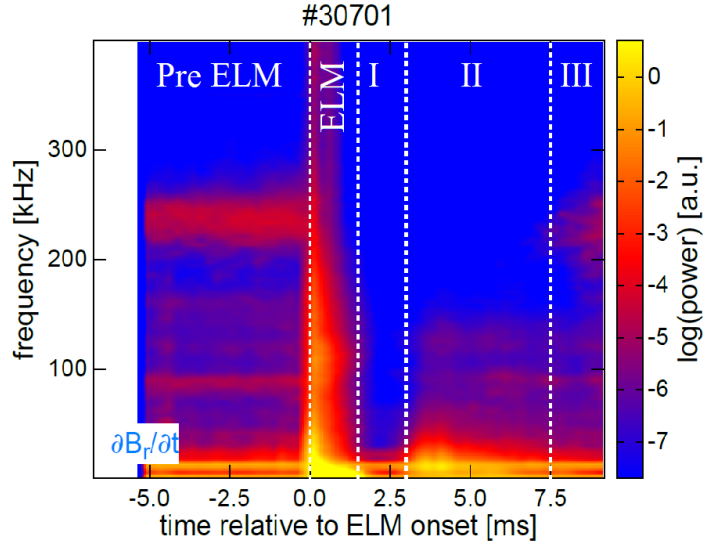

Figure 3.2.: ELM cycle of discharge #30701 from 2.975 s to 3.4 s. The cycle is classified into three distinct phases corresponding to their magnetic behaviour. Figure taken from [24].

After the ELM crash, which is characterized by a broadband fluctuation from 0 ms to ~1.5 ms, the *quiet* phase or phase I occurs. Compared to the other phases there are no magnetic fluctuations observed except for the low frequency ones.

In phase II mid-frequency fluctuations with frequencies about 50 - 150 kHz appear which are supposed to be responsible for additional particle transport into the SOL [13]. This interpretation comes from an increased D_α signal at the divertor which is accompanied by an increase in the divertor electron density [12]. The onset of high-frequency fluctuations (180 - 250 kHz) characterizes phase III where both density and temperature reach pre ELM values.

In this thesis the classification of the phases remains always the same and the timebase is shown in table 3.1.

Phase	t_{beg} [ms] to t_{end} [ms]
Pre ELM	-7 to 0
ELM	0 to 1.5
I	1.5 to 3
II	3 to 7.5
III	7.5 to 15

Table 3.1.: Timebase for the distinct phases relative to ELM onset (t - t_{ELM} = 0 ms) during the ELM cycle of discharge #30701. The ELM itself was assumed to have a duration of 1.5 ms.

The electron density at different radial positions during the ELM cycle is shown in figure 3.3. Because of the ELM crash particles are expelled to the scrape-off layer and the density decreases abruptly in the pedestal.

In phase I the density profile recovers fast. Low transport is expected in this phase because of fast density recovery. In phase II the rate of density recovery is reduced. Pre-ELM values for the density profile are reached in phase III.
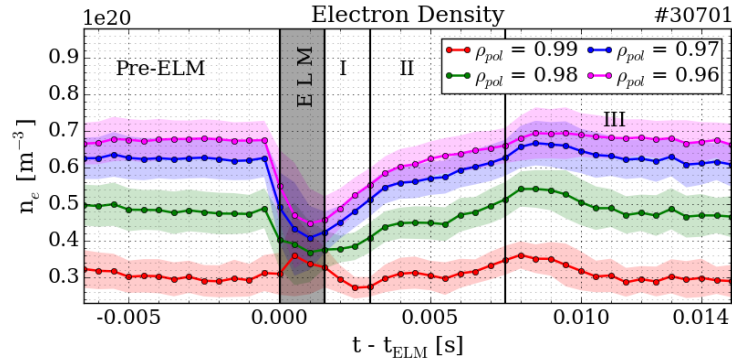

Figure 3.3.: Density at four different radial positions. The curves are colored in magenta for $\rho_{pol} = 0.96$, blue for $\rho_{pol} = 0.97$, in green for $\rho_{pol} = 0.98$ and in red for $\rho_{pol} = 0.99$.

The behavior of the density gradient ∇n_e during the ELM cycle is shown in figure 3.4. The ELM crash at $t_{ELM} = 0$ ms lets the pedestal collapse and flattens the gradients at the plasma edge. The gradients in the pedestal in the beginning of phase I are low and steepen fast during phase I and slower in phase II. At the

same time the density recovery rate is reduced. In phase III the pedestal recovery reaches pre ELM values which are characterized by steep density gradients.
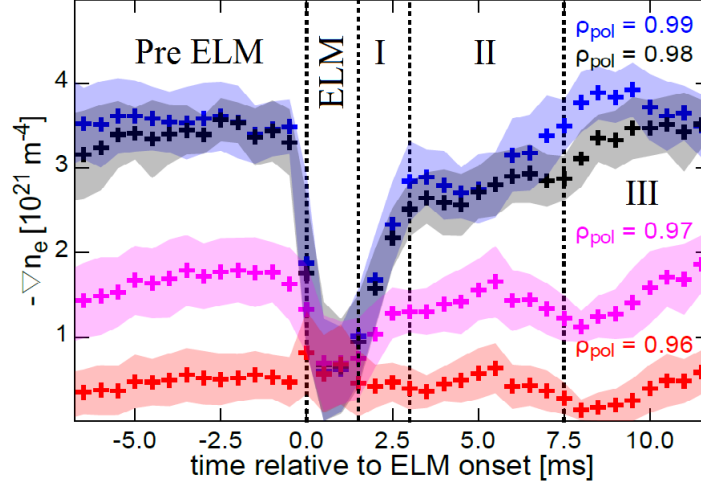

Figure 3.4.: The density gradient at different radial positions. The gradient flattens towards the plasma core. Red and magenta crosses denote ∇n_e at $\rho_{pol} = 0.96$ and $\rho_{pol} = 0.97$, respectively. The gradients for $\rho_{pol} = 0.98$ is shown in black and $\rho_{pol} = 0.99$ is colored in blue. Figure taken from [24].

The temperature profile recovers differently compared to the density profile. After the ELM crash which reduces the temperature, the recovery is slow in phase I. During phase II the recovery rate is increased whereas the density recovery rate stalls. In phase III pre ELM values for the temperature profile are reached.
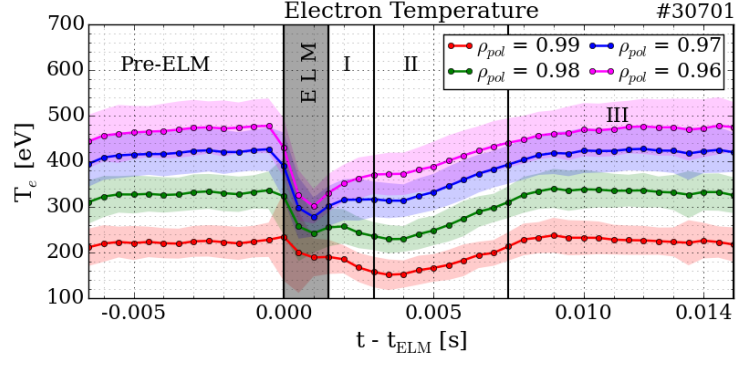
Figure 3.5.: Temperature for four different radial position. The same color code as in figure 3.3) is used. The ELM event can clearly be identified at t - t$_{\text{ELM}}$ = 0 ms.

4. Transport Modeling

In this chapter the model used to calculate the diffusion coefficient is introduced. An overview of the used transport algorithms is given, their intrinsic restrictions are described and their assumptions discussed. Ideas to model and estimate neutral sources at the separatrix are worked out and presented. In the last section the model assumptions are described and summarized.

4.1. The ASTRA Code

ASTRA is an acronym for **A**utomatic **S**ystem for **TR**ansport **A**nalysis. It deals with one-dimensional diffusion equations for densities and temperatures of plasma components and a two-dimensional equilibrium equation. Combination of these two leads to the definition *1.5 dimensional transport code.*

In general it is a flexible programming system [25] with various possibilities to create codes for transport modeling. The model has to be specified in a so called *model file* which specifies assumptions for e.g. particle or energy sources and sinks, boundary conditions or particle pinches. Experimental data is stored in an *experimental file* and can be accessed from the model file. ASTRA takes the given model and the data input to create the transport code. Because of the interactive design input parameters can be changed during the simulation run.

Plug-in subroutines are provided to allow additional considerations like NBI or gas puff neutrals.

ASTRA models are embedded in a toroidally symmetric magnetic configuration and no scrape-off layer physics are included. Quantities like the density of incoming neutrals have to be set as boundary condition at the last closed flux surface. The calculation of processes inside the SOL needs to be done with other methods. In this work this is performed by the kinetic code KN1D which estimates the neutral density at the separatrix (see section 4.2.2).

The plasma itself is assumed to be always in equilibrium as the *Grad-Shavfranov*

equation implemented into ASTRA is not explicitly dependent on time. All terms appearing in the Grad-Shavfranov equation are extracted and inserted from transport equations. This assumption is practicable because equilibrium relaxation processes are much faster than transport processes [25].

A flux surface averaged particle diffusion equation is solved by the code and it derives an effective diffusion coefficient. Implemented transport equations for tokamak plasmas are derived in [26] and represented in a transport matrix. Which transport equation has to be solved, is specified in the model file.

Simulations in this work used the particle balance to express the diffusion coefficient of density, D_n. For the ASTRA code the transport matrix is assumed to have the form shown in equation 4.1.

$$
\begin{pmatrix} \frac{\Gamma_e}{n_e} \\ \frac{q_e}{n_e T_e} \\ \frac{q_i}{n_i T_i} \\ V'G_1 \frac{\mu_0 j_{\mathrm{BS}}}{B_{\mathrm{p}}} \end{pmatrix} = -V'G_1 \begin{pmatrix} D_n & D_e & D_i & D_E \\ \chi_n^e & \chi_e & \chi_i & \chi_E^i \\ \chi_n^i & \chi_e^i & \chi_i & \chi_E^i \\ C_n & C_e & C_i & 0 \end{pmatrix} \cdot \begin{pmatrix} \frac{1}{n_e} \frac{\partial n_e}{\partial \rho} \\ \frac{1}{T_e} \frac{\partial T_e}{\partial \rho} \\ \frac{1}{T_i} \frac{\partial T_i}{\partial \rho} \\ \frac{E_\parallel}{B_p} \end{pmatrix} \tag{4.1}
$$

Flux surface averages are included by the factor $V'G_1$ on the right hand side of this equation. In this equation ρ is the toroidal magnetic flux coordinate of a magnetic surface.

The equation for the diffusion coefficient implemented into the model file yields

$$
D_n = \frac{\Gamma_e}{G_{11} \partial n_e / \partial \rho} + C_n n_e \frac{\partial n_e}{\partial \rho} \Theta(0.85 - \rho) \tag{4.2}
$$

in which $G_{11} = -V'G_1$. A pinch with velocity C_n which is defined up to $\rho = 0.85$ is also added to the model to achieve better matching of modeled and experimental density profiles in the core. The heaviside function $\Theta(\xi < 0) = 0$ is zero if its argument ξ is smaller than zero and $\Theta(\xi \geq 0) = 1$ for arguments $\xi \geq 0$ greater and equal zero.

The output is converted to normalized poloidal flux coordinates ρ_{pol}.

$$
\rho_{pol} = \sqrt{\frac{\Psi - \Psi_a}{\Psi_s - \Psi_a}} \tag{4.3}
$$

The flux Ψ at the separatrix is denoted by Ψ_s and at the magnetic axis it is Ψ_a. Two ways of calculation are possible. ASTRA can be used either interpretatively or in predictive mode. In predictive modeling density and temperature

profiles are calculated from model considerations, which can be compared to experimentally measured data, and interpretative modeling provides quantities (e.g. diffusion coefficient) derived from experimental profiles.

4.2. Consideration of Neutrals

In previous chapters the focus on neutrals in this work is mentioned. The ASTRA code package is equipped with a subroutine *NEUT* that includes an incoming neutral flux into the confined plasma. Thereby a mono-energetic neutral density with corresponding delta distributed energy has to be set as a boundary condition at the separatrix. The particles enter the plasma, get ionized and are added to the plasma.

These neutrals have to be distinguished from the fast ones injected by the NBI as they penetrate much deeper into the plasma. The fueling from the NBI is mainly located at the core and not of interest in this study. Therefore it will further be neglected.

Two mono-energetic species (denoted as *warm* and *cold*) can be considered with different densities. Their energy is delta distributed at arbitrary values. The mass of neutral particles is assumed to coincide with the mass of the working gas.

In this investigation only neutrals with one energy are included and their energy and density is varied.

Due to the difficulty to calculate the behaviour of the neutrals from the wall to the confined plasma region an introduction of different *neutral regimes* is made. They are based on the pressure gauge signal M17 at the midplane and D_α signals at the outer divertor. An explanation is given in the following sections but at first the cases are only generally introduced

A) During the ELM cycle the neutral source is constant in time.

B) The signal of the midplane gauge M17 is processed with the KN1D code.

C) The D_α signal at the outer divertor was used to indicate the time dependent neutral source

D) A modification of the very same D_α signal, where no neutrals during the ELM are assumed, is used.

The neutral density at the separatrix is assumed to be constant for only one type of simulation. For three other different cases it is changing over time. These four distinct cases are investigated and also compared to each other. The letters A, B, C, D labeling these regimes are kept in further descriptions.

The following sections give a deeper insight into the different considerations for the neutral particles in the four cases. The resulting functions serving as ASTRA input for the time dependent neutral sources are also described there.

4.2.1. Constant Neutral Density Source - Case A

The neutral regime A assumes a constant density source n_0 during the whole ELM cycle. The density is varied by multiplication of a fixed constant density with a factor α. The source is assumed to be $n_0 = \alpha \cdot 0.7 \cdot 10^{16}$ m^{-3}. The value for $\alpha = 1$ is taken from the one dimensional KN1D simulation of the scrape-off layer. In the section for case B (page 31) this is explained in detail. What finally serves ASTRA as input for a constant neutral density without scaling is shown in figure 4.1.
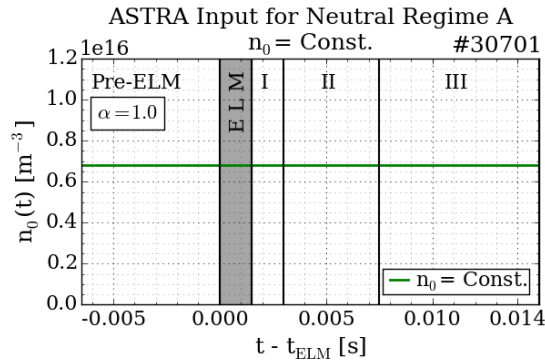

Figure 4.1.: A constant neutral density at the separatrix serves as input to the subroutine NEUT to take neutrals into account. In this case the density is not scaled ($\alpha = 1$).

For different simulations the absolute value of n_0 is multiplied by a factor α. If no scaling is applied, then $\alpha = 1$. The values of α that are multiplied with the constant density function are shown in table 4.1.

Scaling Factor α
0.1
0.5
1.0
1.5
2.0
5.0
10.0

Table 4.1.: Values of the scaling factor α. The density for no scaling ($\alpha = 1.0$) is the result obtained from KN1D in the Pre-ELM phase of the ELM cycle.

The energy of the incoming neutrals can also be selected in the subroutine NEUT. The values that are used for the energy of the incoming neutrals are shown in table 4.2.

Neutral Energy E
2 eV
3 eV
5 eV
8 eV

Table 4.2.: Values of E for incoming neutrals. The values of energetic neutrals with 3 eV and 5 eV are assumed to rely on Franck-Condon dissociation processes. This is described in section 2.3. In order to obtain a greater energy spectrum the values 2 eV and 8 eV are investigated as well.

In the simulations for all neutral regimes (A,B,C,D) both parameters α and E are varied independently of each other.

4.2.2. Midplane Signal - Case B

To estimate the neutral density at the separatrix the kinetic transport algorithm KN1D is used. It basically calculates distribution functions for molecular and

atomic hydrogen or deuterium. The code is one dimensional and calculates several plasma quantities (e.g. molecular and atomic temperature, atomic ionization rate, heat fluxes and so on) in the SOL at the midplane.

The spatial geometry, on which this simulation is based, is slab-like and can be further specified in the *input file*. Thereby wall surface, limiter shadow, scrape-off layer and confined region are taken into account. Apart from the geometric dimensions the plasma profiles and the molecular neutral pressure are serving as input.

The KN1D model assumes particles to be born at the vessel wall as molecular deuterium at room temperature (0.025 eV) with an isotropic Maxwellian distribution function. Several dissociation, exciation and ionization processes are included in scrape-off layer simulations and are described in more detail in [27]. The data of the pressure gauge for the input file is obtained from the midplane gauge M17. The thereby measured and ELM synchronized particle flux is shown in figure 4.2. Due to calibration reasons the curve is shifted by -1.5 ms [24].
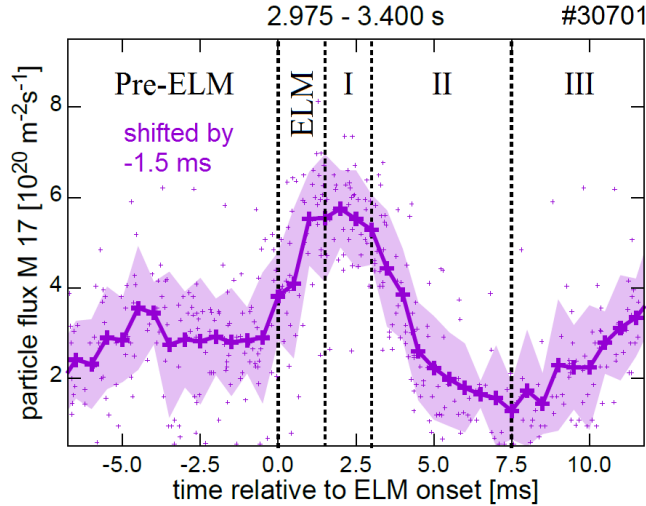

Figure 4.2.: ELM synchronized particle flux measured at the midplane vessel wall. The curvature is shifted by -1.5 ms. Picture taken from [24].

In the input file the density and temperature profiles used in the KN1D calculation are the same as the ones used for the ASTRA calculations inside the plasma. Because of the difficulty to obtain reliable temperature profiles in the SOL, it is adapted by an exponential decay in this region with a decay length λ = 6.5 mm [16]. To model shot #30701 deuterium is selected to be recycled at

the wall.

The output of the KN1D calculation for atomic neutral density at the separatrix is shown in figure 4.3. The value for $n_{0,KN1D}$ in the pre ELM phase doesn't fluctuate much from -0.0045 to -0.0005 s relative to the ELM onset. Therefore averaging these values leads to a comparatively small error. The value of the density is generally based on this average and further scaled with the scaling factor α. The average $\langle n_{0,KN1D} \rangle$ is determined to be $\langle n_{0,KN1D} \rangle = 0.68 \cdot 10^{16}$ m^{-3}. All further neutral density regimes are assumed to match this KN1D result in the pre ELM phase if no scaling is applied.
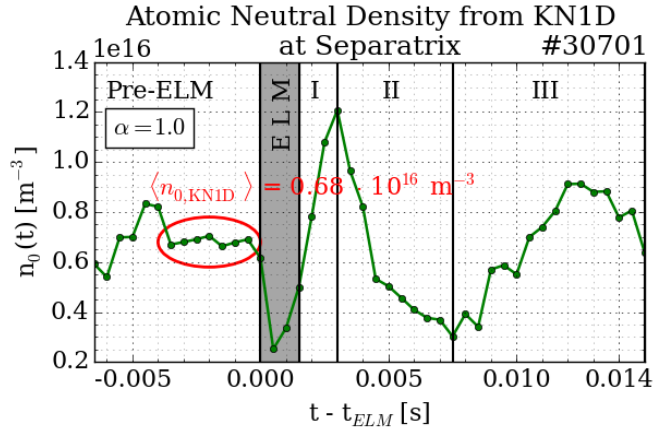

Figure 4.3.: Match of the KN1D result to the ASTRA input. The mean value $\langle n_{0,KN1D} \rangle$ is calculated in the interval illustrated with a red ellipse.

The ASTRA model of the neutral density behavior for case B is shown in figure 4.4. No scaling is applied ($\alpha = 1$) and the values are directly comparable to the result of the KN1D calculation.
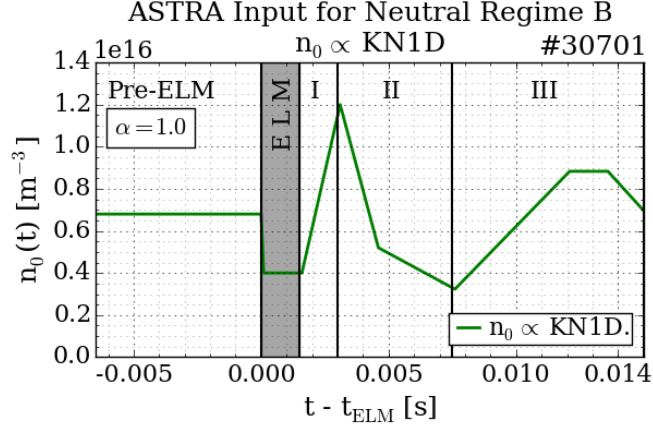
Figure 4.4.: The input of the neutral source to the ASTRA code for neutral regime B without scaling ($\alpha = 1$) is shown.

4.2.3. D_α Signal at the Divertor - Case C

Photons are emitted if electrons fall to a lower state of energy in excited atoms. In hydrogen, the energy of the emitted photon depends in first order on the principal quantum number of initial n_i and final state n_f. The transition from n=3 → n=2 is called α-line of the Balmer series.

As for this effect an electron has to be bound to the core, the D_α signal is assumed to be somehow related to a neutral density. The intensity of I_{D_α} depends on the number of neutrals in the excited state n=3, $I_{D_\alpha} \propto n_0(D(n = 3))$. The excited state is nonlinearly dependent on not only the neutral density but also the electron density and temperature. However, no quantification for this general assumption is undertaken in this work.

The D_α signals are measured spectroscopically at the outer divertor. The signal is shown in figure 4.5. A second peak after the ELM crash develops which could also be observed earlier [28] and even at different tokamak experiments [29]. It is excluded that this behaviour comes from a second ELM because the temperature doesn't increase simultaneously [28]. Its origin is currently explained by a higher particle flux into the SOL due to the mid-frequent fluctuations [13]. This leads to higher recycling at the divertor and therefore to higher neutral production.
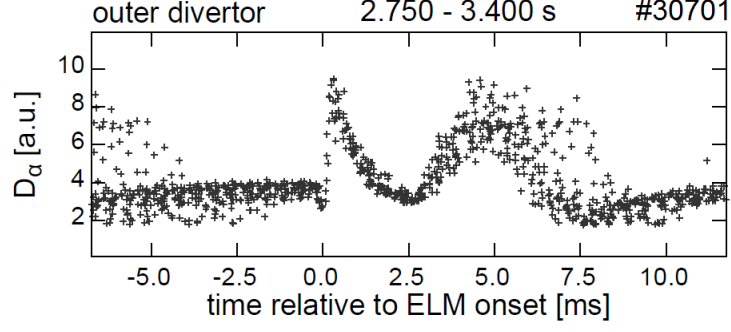
34

Figure 4.5.: D_α signal at the outer divertor measured by spectroscopy. After the ELM peak at t - t_{ELM} = 0 ms a second peak evolves. The D_α signal is assumed to be somehow related to a neutral density at the midplane. Figure taken from [24].

The signal is interpreted qualitatively as neutral density and combined with the averaged KN1D result in the pre ELM phase by matching the values (n_0^{PRE} = $\langle n_{0,KN1D} \rangle$). This is also described in the previous section. For the neutral regime C the function $n_0(t)$ is assumed to have the same shape as the one of the outer divertor D_α signal. The amplitude of the peaks is estimated relatively to the pre-ELM value and in this way the function of D_α is rebuilt as neutral source. With n_0^{PRE} = $\langle n_{0,KN1D} \rangle$ the model can be based on quantitative values. Processes that impact neutrals on their way to the separatrix at the midplane are neglected.

The modeled function of the neutral density that serves as input for the ASTRA code is shown in figure 4.6.
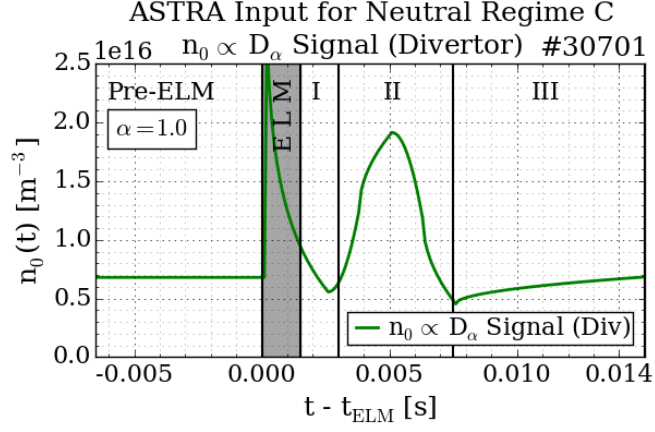
Figure 4.6.: The D_α signal at the outer divertor is taken to indicate the neutral source. An exponential decay of the neutral source after the ELM onset is modeled. The second peak is approximated by parabolic functions.

4.2.4. Modification of the Divertor Signal - Case D

In the fourth neutral regime D, it is assumed that no neutrals are crossing the SOL during the first 0.5 ms after the ELM onset. This is related to the high density and temperature outside the separatrix during the ELM event [28]. In the model the neutral source increases linearly after 0.5 ms after the ELM until the end of phase I and is then matched with the D_α signal like in neutral regime C.

The function that is used in the ASTRA simulations is shown in figure 4.7. On the contrary to the cases A,B,C the average of the neutral density in phase I ins lower than $n_{0,PRE}$. An estimation yields $n_{0,I} \sim 0.6 \cdot n_{0,PRE}$.
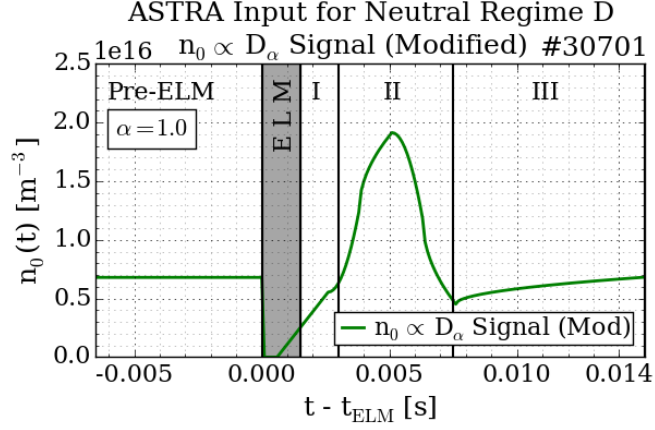
Figure 4.7.: Identical D_α signal taken to model the neutral source. During the ELM no neutrals are assumed due to the dense SOL. A linear increase from 0.5 ms after the ELM until phase II is assumed.

Although the assumptions to model the neutral regimes C and D are quite arbitrary they are used in simulations to give an estimate of how neutrals impact the determination of the diffusion coefficient. Further scrape-off layer modeling has to be taken into account if more reliable results are desired.

4.3. Model Assumptions and Input Profiles

The actual input profiles for the ASTRA simulations are presented in this section. General assumptions that have to be considered are also described here.

For the ASTRA simulations experimental density and temperature profiles are used. They are ELM synchronized and divided into distinct phases as described earlier in section 3.3. In general full density and temperature profiles up to the core are necessary.

For the modeling density and temperature profiles are provided each 0.5 ms. The radial grid of these profiles is not equidistant and has more points in the pedestal region. It is interpolated automatically by the ASTRA code.

The density profile for four different phases is shown in figure 4.8. The reduction of the value of the profile due to the ELM can clearly be seen. Because no scrape-off layer physics are considered in ASTRA this region is excluded (gray area). In phase III the pedestal is restored and the profile is almost identical to the one of the pre-ELM phase.
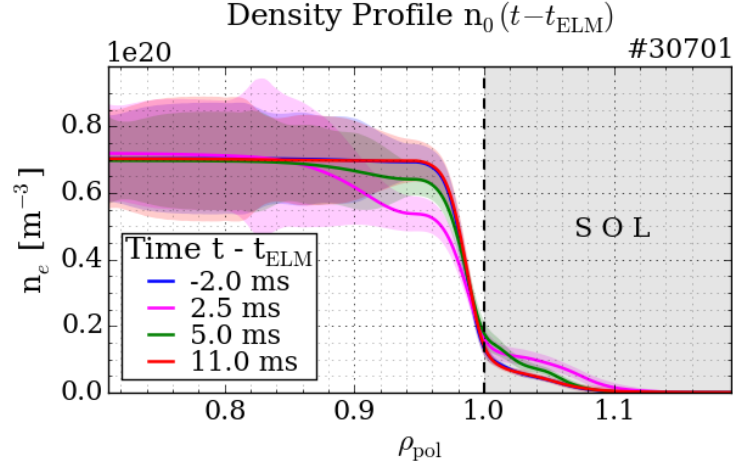
Figure 4.8.: Density profile at four different time steps. The profile in the pre-ELM phase (-2.0 ms) is colored in blue. In phase I (2.5 ms) the curve is colored magenta. Green color is used for phase II (5.0 ms) and a red one for phase III (11.0 ms).

Parts of the used temperature profiles are shown in figure 4.9. The radial grid of the temperature profile for the ASTRA input is identical to the one of the density profile. Because of the difficulty to measure the temperature profile outside the separatrix with the ECE spectrometer the uncertainty of the data is increased (see section 3.1.2).
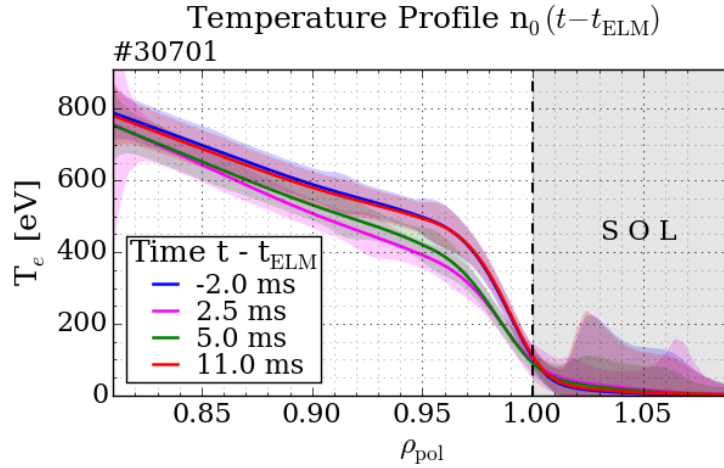

Figure 4.9.: Temperature profile in four different phases. The colors are the same as in figure 4.8.

The high collisionality ($\nu^* > 1$) of the plasma in discharge #30701 allows to set the ion temperature equal to the electron temperature, $T_i = T_e$.

During the ELM crash the equilibrium changes and the plasma volume is reduced by about 3% at maximum which can be seen in figure 4.10.
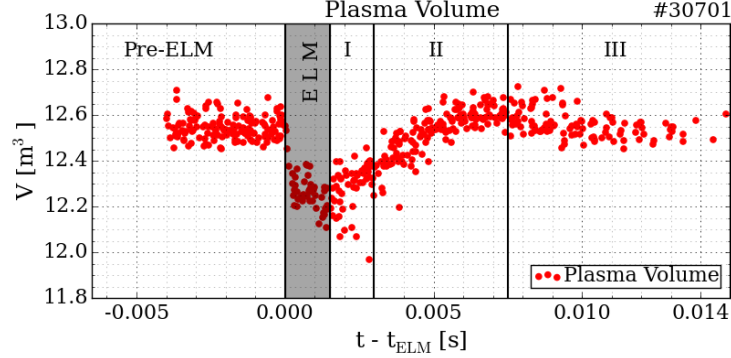

Figure 4.10.: ELM synchronized plasma volume. During the ELM crash the volume shrinks and recovers fast during phase I.

The plasma surface therefore also shrinks. It recovers during phase I and II (1.5 ms - 5 ms relative to ELM) and can have a quantitative impact on the diffusion coefficient as it has units of m^2s^{-1}. The equilibrium in the model used for this study is taken to be constant even during the ELM crash and the volume is not changing.

Because the considered neutrals are not based on exact quantitative calculations an assumed constant equilibrium is not fatal [30]. The effect of the volume reduction is smaller than the estimated source of the density, which is more or less estimated in this work. As soon as this issue is overcome and exact calculations for neutrals are performed, careful consideration of the equilibrium is necessary to get more reliable results.

5. Simulation Output

In this section the output of the ASTRA simulations is presented. The behavior of the diffusion coefficient for different assumptions of the neutral source is described. An interpretation and discussion of the results is given in the following chapter 6.

As mentioned before the subroutine *NEUT* is used to take the neutrals into account. Although an investigation of two distinct neutral densities with different delta distributed energies is possible only one species is investigated.

In all different kinds of simulations presented in this work the average of the diffusion coefficient in each phase is taken with the formula $(D^{0.97}+D^{0.98}+D^{0.99})/3$. Thereby the mean of the diffusion coefficient at each radial position $D^{\rho_{pol}}$ is taken over 2 ms in each phase (in phase I it is averaged over 1 ms).

5.1. Constant Neutral Source (A)

The results of simulations that assumed a constant neutral density are presented and discussed. This is denoted as neutral regime A in this work. As described in section 4.2 a variation of neutral energy E and neutral density via a scaling factor α has been performed.

Beginning to discuss some general results figure 5.1 shall serve as an example. It shows the diffusion coefficients D at ρ_{pol} = 0.97 - 0.99 for E = 3 eV with a constant neutral density of $1.4 \cdot 10^{16}$ m^{-3} (α=2) at the separatrix. Disregarding the absolute value for D_{PRE}, which is significantly lower compared to estimations in [18] that finds $D \sim$ 0.1 - 0.25 m^{2}s^{-1}, some qualitative behaviour can be seen. A quantitative consideration is undertaken later in section 5.1.3.
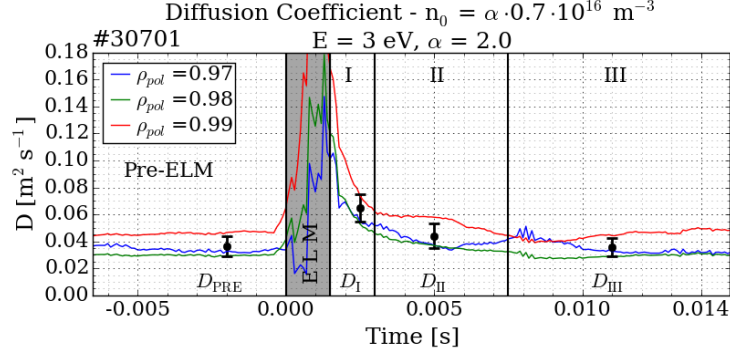
Figure 5.1.: Example calculation for the diffusion coefficient with a constant neutral source. The diffusion coefficient is shown for three radial positions. $D^{0.99}$ is colored in red, $D^{0.98}$ in green and $D^{0.97}$ is painted in blue. During the ELM no reliable result is achieved and therefore it is excluded from consideration. This is illustrated by the gray shaded area from $t_{ELM} = 0$ ms to 1.5 ms.

The diffusion coefficients in the phase after the ELM crash D_I shows a decay-like behavior if a constant neutral source is applied. D_I is higher in phase I than in the pre-ELM phase and further decreasing to pre-ELM values again. This behavior is observed for all varied parameters of all simulations assuming a constant neutral density during the ELM cycle. Changing the energy and density doesn't change the qualitative characteristic of the curves shown in figure 5.1. In the following sections the impact of the variation of the neutral energy and density is investigated separately.

5.1.1. Impact of Neutral Energy

In table 4.2 the values of the energy used for the simulations are shown. To show the impact on the diffusion coefficient independently of the neutral density, the density is not changed for this kind of investigation. No scaling is applied ($\alpha = 1$) and the absolute value for the density is set to a constant value of $0.7 \cdot 10^{16}$ m^{-3}. The energy is varied for the parameters E = 2, 3, 5, 8 eV.

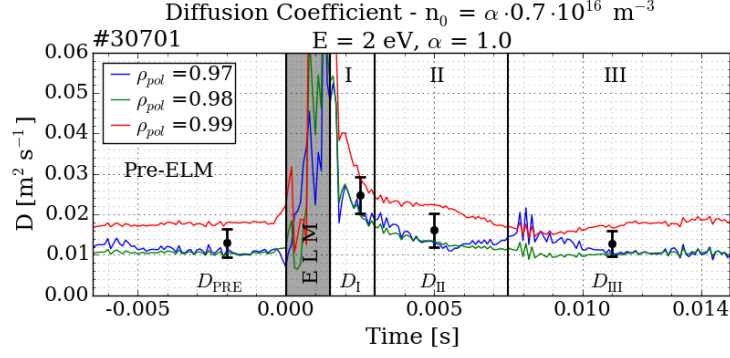The two cases at the limits of the energy variation (2 eV and 8 eV) are particularly discussed in this section.

Figure 5.2.: Diffusion coefficients for a neutral energy of 2 eV and a constant density $n_0 = 0.7 \cdot 10^{16}$ m^{-3} ($\alpha = 1.0$). The color code is identical to figure 5.1 The curve for $D^{0.99}$ (red) is distinguishable from the others which have similar values.

In figure 5.2 the diffusion coefficients are shown for a neutral energy of 2 eV and a constant density $n_0 = 0.7 \cdot 10^{16}$ m^{-3} ($\alpha = 1.0$). D shows almost equal values for ρ_{pol}=0.98 and ρ_{pol}=0.97. $D^{0.99}$ is separated from the others. It is expected that a higher neutral energy affects the diffusion coefficient deeper in the confined region. The comparison of $D^{0.97}$ and $D^{0.98}$ confirm this behavior. This is shown in table 5.1.

E	$D_{PRE}^{0.97}$ [m^{2}s^{-1}]	$D_{PRE}^{0.98}$ [m^{2}s^{-1}]	$D_{PRE}^{0.97}/D_{PRE}^{0.98}$
2 eV	0.010	0.010	1.0
3 eV	0.016	0.015	1.07
5 eV	0.026	0.022	1.18
8 eV	0.039	0.031	1.26

Table 5.1.: Comparison of D_{PRE} for radial position $\rho_{pol} = 0.97$ and $\rho_{pol} = 0.98$. The ratio between these two is increasing for higher energies. The quantitative values are lower than previously estimated in [18] but can be arbitrarily scaled (see section 5.1.2).

In table 5.1 calculated values for D_{PRE} are shown for different energies. The total value as well as the ratio increases for higher energies. This is in accordance with a higher neutral density at higher energies for a given radial position.

To give an illustration figure 5.3 is shown. All parameters remain unchanged and only the energy is increased to 8 eV. For this case the diffusion coefficients at ρ_{pol}=0.98 and ρ_{pol}=0.97 are also separated. A higher total value of D can also be observed.
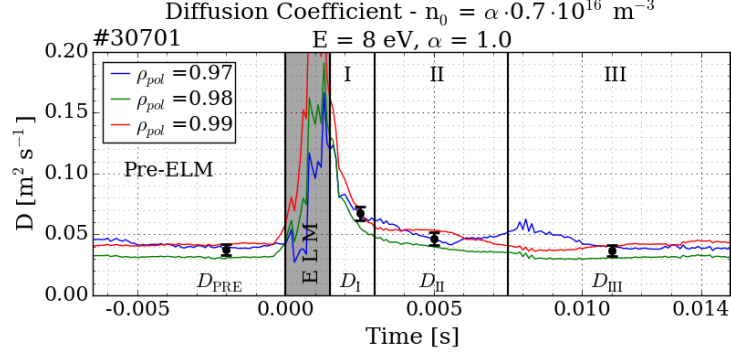

Figure 5.3.: T same calculation but for higher neutral energy (8 eV) is shown in this figure. In comparison to the lower energetic case (2 eV) the diffusion coefficients deeper inside the plasma fan out due to higher neutral penetration depth. The colors are the same as in figure 5.1.

The reduction of the neutral density inside the plasma due to ionization processes is shown in figure 5.4. This calculation is done in the pre-ELM phase at -0.002 s relative to the ELM onset. It is clear that this is consistent with previous arguments as for a given ρ_{pol} the neutral density is higher for higher energies. Quantitatively, it can be seen that $n_0^{0.97}$ is about 25% higher for 8 eV than for 2 eV.
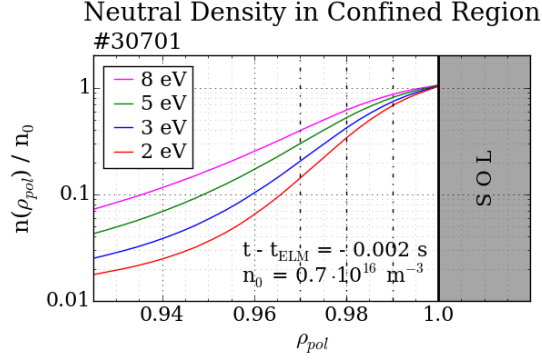
Figure 5.4.: Radial profile of neutral density normalized to the value at the separatrix. A higher energy enables a neutral particle to fly deeper into the confined region. The calculation is done at -0.002 s relative to the ELM onset normalized to a constant density of $0.7 \cdot 10^{16}$ m^{-3}. The highest energy, 8 eV is colored in magenta, 5 eV is green, 3 eV is blue and 2 eV is red.

To sum things, up it is shown that the energy of neutrals has an impact on the radial dependence of D. The total value of D is also increasing with increasing E. In the next section the neutral density is varied for a fixed constant energy.

5.1.2. Impact of the Scaling Factor α

For these calculations the neutral energy is set to a constant value of 3 eV. The density is varied by multiplying the value $n_0 = 0.7 \cdot 10^{16}$ m^{-3} with a scaling factor α. It ranges from 0.1 to 5.0. The cases $\alpha = 0.1$ and $\alpha = 5.0$ are directly compared in this section.

In figure 5.5 the diffusion coefficient is shown for a constant neutral density of $0.7 \cdot 10^{15}$ m^{-3} ($\alpha = 0.1$). The value for D_{PRE} is ~ 0.002 m^{2}s^{-1} which is about one order of magnitude lower than for the case with $\alpha = 1.0$.
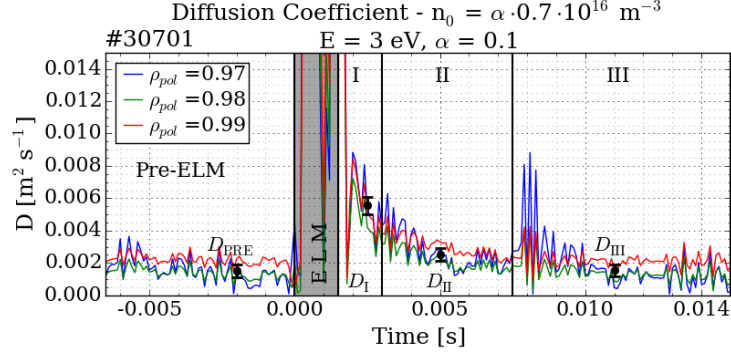
44

Figure 5.5.: Diffusion coefficients for a constant density of $0.7 \cdot 10^{15}$ m^{-3} ($\alpha = 0.1$) and a neutral energy E = 3 eV. The color code is identical to figure 5.1.

Figure 5.6 shows the results for the neutral density increased to $3.5 \cdot 10^{16}$ m^{-3} ($\alpha = 5.0$). The value for D_{PRE} is about 2 orders of magnitude higher compared to the case with $\alpha = 0.1$. The total value for D is significantly higher for higher neutral density but the radial dependency is not clearly affected. Despite the increasing absolute value of D its temporal behavior remains unchanged.
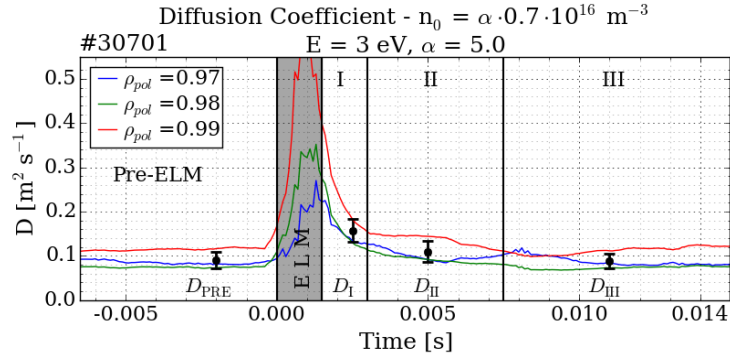
Figure 5.6.: Calculation for D with constant neutral source for a $\alpha = 5.0$ and a constant energy at E = 3 eV. The absolute value for D is increased equally for all radial positions. The color code is identical to figure 5.1.

In table 5.2 the values of D_{PRE} at E = 3 eV are shown for all α investigated in this simulation series. The diffusion coefficient is increasing for increasing density. If the slope can generally be assumed to be linear is discussed in the next section.

α	D_{PRE} [m^{2}s^{-1}]
0.1	0.0015
0.5	0.0088
1.0	0.0179
1.5	0.0270
2.0	0.0361
5.0	0.0908

Table 5.2.: Diffusion coefficient in the pre-ELM phase for E = 3 eV.

5.1.3. Combination of Results

In this section a summary plot for D_{PRE} for all investigated values of α and the neutral energy E is given. The neutral density at the separatrix is assumed to be $n_0 = \alpha \cdot 0.7 \cdot 10^{16}$ m^{-3}. An overview plot is shown in figure 5.7. Different colors denote the diffusion coefficient at different neutral energies.

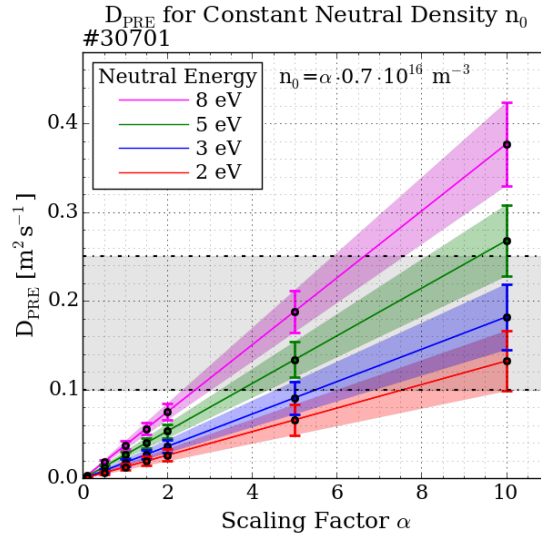Figure 5.7.: Overview of D_{PRE} after an independent variation of α and the neutral energy. The color code is identical to figure 5.4. The gray background illustrates the total value for D_{PRE} calculated by [18, 31].

The gray area in figure 5.7 indicates the previously modeled value for D_{PRE}. Chankin et al. [18] estimate $D_{\mathrm{PRE}} \sim 0.1$ - 0.25 m^{2}s^{-1}.

Different ionization, dissociation and charge exchange processes lead to a production of energetic neutrals in the SOL (see page 16). For neutrals with energies of 3 eV (blue) their density has to be about $4.2 \cdot 10^{16}$ m^{-3} ($\alpha = 6.0$) to lie within the gray area. More energetic neutrals need to be less dense to reach the same limits.

To investigate the slope of the curves shown in figure 5.7 and decide whether it is linear or not for small values further considerations are made. By taking the ratio

$$k_i = \frac{D_{\mathrm{PRE}}(\alpha_{i+1}) - D_{\mathrm{PRE}}(\alpha_i)}{\alpha_{i+1} - \alpha_i} \tag{5.1}$$

for the curve of one energy and iterative comparison of all k_i, a possible change in the slope can be detected. The values of all k_i for for each energy are averaged and shown in table 5.3. Comparison of the values show no *exact* linearity, because the standard deviation $\sigma(k)$ of the average $\langle k_i \rangle$ is not 0. It is found that $\sigma(k)$ is small and may also come from numerical uncertainties. The increasing error for lower energies might indicate a non linear slope for low energies of the neutral source. However, from the data points obtained in this work the curves are assumed to be linear.

E [eV]	$\langle k_i \rangle$ [m^{2}s^{-1}]	$\sigma(k)$ [m^{2}s^{-1}]
2	0.0132	$2.28 \cdot 10^{-5}$
3	0.0182	$1.12 \cdot 10^{-6}$
5	0.0268	$8.72 \cdot 10^{-7}$
8	0.0377	$2.00 \cdot 10^{-7}$

Table 5.3.: The average slope $\langle k_i \rangle$ of the diffusion coefficient D_{PRE} at different energies is calculated.

In further calculations(cases B, C and D) with time dependent neutral sources the energy is set to 3 eV and the neutral density in the pre ELM phase n_0^{PRE} = $5.6 \cdot 10^{16}$ m^{-3} ($\alpha = 8.0$). A common value for all neutral regimes for D_{PRE} is achieved this way.

5.2. Time Dependent Neutral Source

In this section the results for a time dependent neutral density at the separatrix are described. The modeling of the neutral source is described in section 4.2 and only the results are presented here. In the end of this chapter all neutral regimes are compared to each other in a bar diagram.

5.2.1. Neutral Source from KN1D calculation (B)

The result of the diffusion coefficient studies with a neutral source with a time dependency estimated via KN1D calculation is presented here. This is denoted as neutral regime B and the function of the particle source at the plasma boundary is shown in figure 4.4. The parameters α and the neutral energy E are set to 8.0 and 3 eV, respectively ($n_0^{\mathrm{PRE}} = 5.6{\cdot}10^{16}$ m^{-3}). The value for D_{PRE} is then between the limits estimated in [18].

Figure 5.8 shows the result of this calculation at three radial positions.
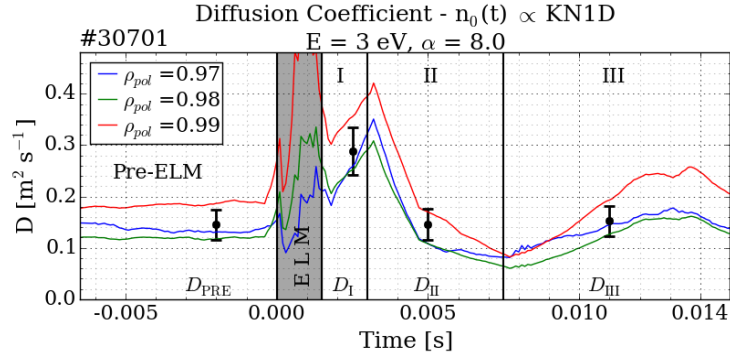
Figure 5.8.: Diffusion coefficient at three different radial positions with a neutral source calculated from KN1D for $\alpha = 8.0$ and E = 3 eV. Color code is identical to figure 5.1).

It can be seen that the neutral source plays an important role in the diffusion coefficient calculation. In phase I D_{I} is increasing due to an increasing neutral source at the same time. The source reduces afterwards, D reduces as well and D_{II} even drops below the D_{PRE} value. Then D increases again and finally reaches the pre ELM level. The averaged values in phases II and III do not vary much.

5.2.2. Neutral Source from D_α Signal (C and D)

Case C

The outer divertor D_α signal is related to a neutral source and the results of the calculations are presented here. For the density in the pre-ELM phase n_0^{PRE} the same value as the one in case B, $n_0^{\mathrm{PRE}} = 5.6 \cdot 10^{16}$ is used. The energy is also set to $E = 3$ eV. The exact function of the neutral source that served as input for these simulation is shown in figure 4.6.
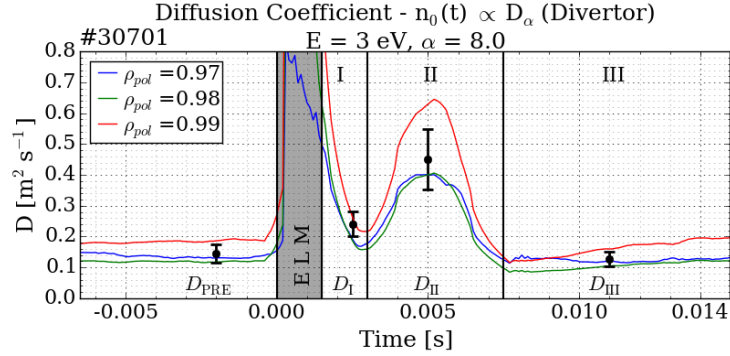

Figure 5.9.: Diffusion coefficient at three different radial positions with a neutral source estimated from the D_α signal of the outer divertor (Case C). The energy is set to $E = 3$ eV and the scaling factor α to $\alpha = 8.0$. Color code is identical to figure 5.1.

In figure 5.9 the results of case C for D at three different spatial positions is shown. As already recognized in previous studies the strong dependence of D on the neutral source is also observed here. After the ELM D_{I} shows an exponential decrease due to the exponentially decaying assumption made for the neutral source in this phase. In phase II a parabolic shape of the diffusion coefficient is observed, which corresponds to the higher neutral density in this phase. At the end of phase III the diffusion coefficient reaches pre ELM values again.

Case D

Finally no neutrals are assumed until 0.5 ms after the ELM onset (Regime D). After a linear increase of $n_0(t)$ from 0.5 ms after the ELM until phase II, this

neutral regime D is identical to regime C (see figure 4.7). The result of the simulation with parameters $\alpha = 8.0$, E = 3 eV is shown in figure 5.10
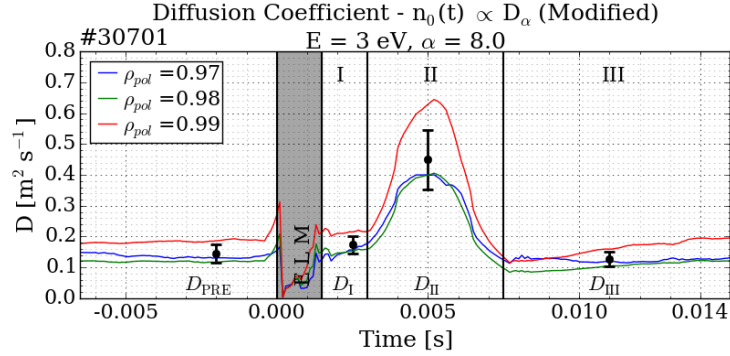

Figure 5.10.: Diffusion coefficient at three different radial positions with a neutral source estimated from the D_α signal without a neutral source during the first 0.5 ms after the ELM (case D). The energy is set to E = 3 eV and the scaling factor α to $\alpha = 8.0$. The color code is identical to figure 5.1.

Due to the assumptions of case D, almost constant behavior of D_I is found in phase I. This is contrary to other results. Nevertheless, the average of D_I is slightly increased compared to D_{PRE}.

5.3. Comparison of Different Neutral Regimes

To compare the previously obtained results an overview for D in different phases for the different neutral regimes is given. Data from the previously discussed results with $\alpha = 8.0$ and E = 3 eV are taken and summarized in one plot. In addition an extra calculation is performed for an assumed neutral source $n_0^{PRE} = 3.5 \cdot 10^{16}$ m^{-3} ($\alpha = 5$) with 5 eV neutral energy.
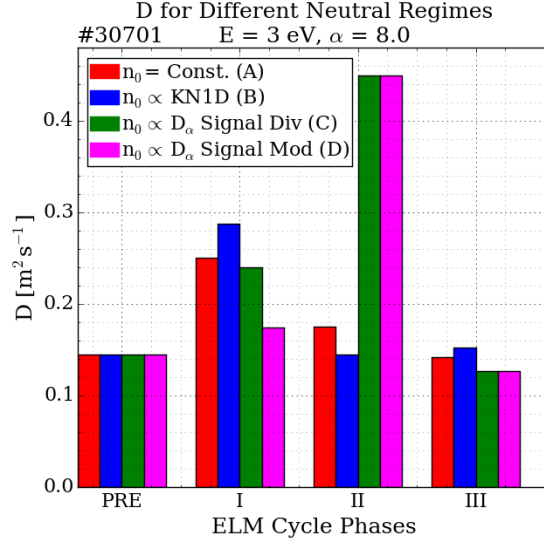
Figure 5.11.: Bar diagram of D in all phases for different neutral sources. The neutral energy is 3 eV and $n_0^{\mathrm{PRE}} = 5.6 \cdot 10^{16}$ m^{-3} ($\alpha = 8.0$). Red bars denote a constant neutral density (case A). Results considering the KN1D calculations are colored in blue (case B). The outer divertor signals are given in green (original signal, case C) and magenta (modified signal, case D).

In figure 5.11 D is shown for $n_0^{\mathrm{PRE}} = 5.6 \cdot 10^{16}$ m^{-3} ($\alpha = 8.0$) and neutral energy E = 3 eV which is identical in all four regimes. This can be seen in figure 5.11 as the bars of the pre ELM-phase are all equal.

Depending on the neutral source assumptions the diffusion coefficient in phase I is increased by about $\sim$ 12 - 100% compared to D_{PRE}. For a constant neutral source it is increased by about 70% (red bar). An interpretation for this behavior in phase I is given in the conclusion in chapter 6.

In phase II which is characterized by the onset of mid-frequency fluctuations a higher particle flux into the SOL is expected because of the increased measured densities and D$_\alpha$ emissions in the divertor. This is observed considering the results of case C and D in figure 5.11. The neutral midplane signal processed with KN1D (blue bar) doesn't show an increased diffusion coefficient during this phase. In general, a strong dependency of D on the assumptions made for the neutral source is observed.

In phase III the diffusion coefficients are recovering to pre ELM values and do not vary much among each other.

A similar summary plot for $\alpha = 5.0$ and E = 5 eV is shown in figure 5.12. Due to the Franck-Condon dissociation process $H_2 + e^- \rightarrow H + H^+$ (5.0 eV) (see itemization on page 16) energetic neutrals with E = 5 eV are also produced. To match $D_{\mathrm{PRE}} \sim 0.1$ - 0.25 m^{2}s^{-1} the scaling factor α is chosen to be $\alpha = 5.0$. It basically shows identical behavior of D with slightly different absolute values and is shown in figure 5.12.
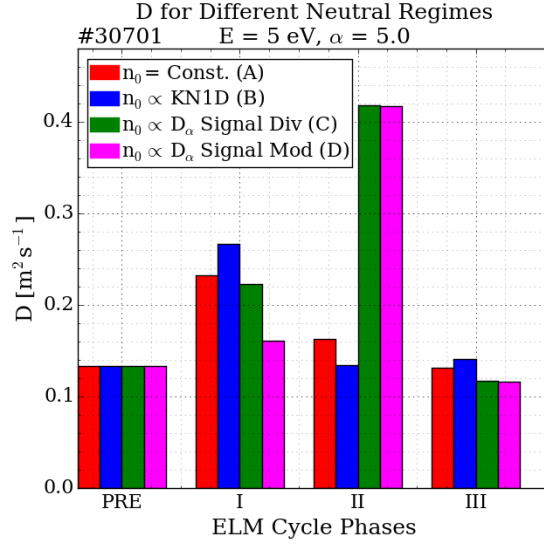
Figure 5.12.: Bar diagram for four different neutral regimes similar to figure 5.11. The neutral energy in this simulation is assumed to be 5 eV and $n_0^{\mathrm{PRE}} = 3.5 \cdot 10^{16}$ m^{-3} ($\alpha = 5.0$). The color code is identical to 5.11.

Comparison of both results yields no generally different behavior. The absolute values of D are lower in the case with lower density ($\alpha = 5.0$) which corresponds to the result described in section 5.1.2.

One concluding result of the study with varying neutral regimes is the importance of the exact knowledge of the neutral source. Reliable calculations for the particle source are indispensable for quantitative studies of the diffusion coefficient. It is not clear which neutral regime is the most reliable one especially for the results of phase II.

6. Conclusion

In discharge #30701 2.975 - 3.4 ms all data were synchronized to the ELM onset. The obtained representative ELM cycle was split into 4 distinct phases (pre ELM, I, II, III) due to the magnetic characteristic. Time dependent transport analysis with ASTRA in interpretative mode were performed to determine the density diffusion coefficient D in different phases of the ELM cycle. A particle source from recycled neutrals was included. Four different cases of neutral temporal behavior were introduced which were related to experimental measurements. The impact due to varying energy and density of the particle source was investigated. The results were compared among each other as well as to previously worked out calculations.

6.1. Results

In this section the most important results of this work are summarized. Calculations were performed for four different assumptions for the neutral density at the separatrix, denoted as neutral regimes A,B,C and D.

Simulations with constant neutral density during the whole ELM cycle (case A) were performed. The neutral density and energy were varied separately and the impact of this variation on the diffusion coefficient was investigated independently.

The increase of the neutral energy E leads to an increase to the diffusion coefficient and changes the radial dependency of D. The augmented energy affects D deeper inside the plasma. This is consistent with the result which was found for the density profile of neutral particles inside the plasma. The comparison for higher energetic neutrals to lower energetic ones shows an increased density for the higher energetic ones at the same radial position. For example, the neutral density at $\rho_{pol} = 0.97$, $n_0^{0.97}$, was found to be 25% higher for 8 eV than for 2 eV. The impact of the neutral energy on the diffusion coefficient was shown with

these investigations.

Independently from the energy the neutral density was varied by multiplication of the density with a scaling factor α. Higher neutral densities (higher α) showed an increase of the diffusion coefficient whereas the radial dependency of D is not clearly affected.

The values of the diffusion coefficient in the pre-ELM phase D_{PRE} for independent variation of the two parameters α and E was shown in an overview plot. Thereby the increase of D_{PRE} due to an increase in α was shown. The slope of this increase is depending on the neutral energy E. The slope, derived from the available results, shows linear behavior within the limits of uncertainty.

One general result of these simulations is that the absolute value of D cannot be determined without accurate knowledge of E and n_0. Therefore, the diffusion coefficient was compared to previously obtained results [18, 31] that estimate D_{PRE} to be $\sim$ 0.1 - 0.25 $\mathrm{m}^2\mathrm{s}^{-1}$. The scaling factor α and the neutral energy E could then be chosen reasonably to get results for D_{PRE} that lie in between these limits. Thereby the cases $\alpha = 8.0$, E = 3 eV and $\alpha = 5.0$, E = 5 eV were taken as parameters for further calculations with a time depending neutral source $n_0(t)$.

The temporal behavior of the diffusion coefficient was investigated for different phases in the ELM cycle. Thereby the neutral source was set to constant values (case A) or modeled as time-dependent function $n_0(t)$ (cases B,C,D). The model for the neutral source was based on measurements at the midplane and at the outer divertor.

In the pre-ELM phase D_{PRE} has the same values for all neutral regimes A,B,C,D due to identical assumptions of the neutral source in this phase and usage of the same parameters α and E.

The diffusion coefficient in phase I, D_{I}, was found to be larger than D_{PRE} for all neutral regimes. This could also be observed in case D where $n_{0,\mathrm{I}} \sim 0.6 \cdot n_{0,\mathrm{PRE}}$. An interpretation of a possible mechanism that causes this behavior is given in section 6.2.

D in phase II showed strong dependency of the absolute value of D on the assumptions made for the neutral source. The value is similar for cases A and B but about a factor of 3 higher for the cases C and D (which are identical in this phase of the ELM cycle). This higher diffusion coefficient results from the increased neutral density in phase II for cases C and D. As more particles appear

as source in the pedestal, the modeled D must increase to match the measured gradient.

In phase III the values for D are similar for all neutral regimes and the absolute value is about the same as that for the pre-ELM phase.

As mentioned before, the temporal behavior of D was investigated for two sets of parameters ($\alpha = 8.0$, E = 3 eV) and ($\alpha = 5.0$, E = 5 eV). The results didn't change qualitatively, only the absolute values of D are found to be lower, corresponding to the results found by the variation of α and E.

Qualitative statements about the time dependence of the diffusion coefficient D could be made, but it was found that as long as the neutral energy and density are not determined accurately, the absolute value of D cannot be derived.

6.2. Interpretation

To interpret the results for D_I a deeper insight into the mechanism of transport reduction for high confinement operation is necessary. After the discovery of the H-mode 1982 [8] different models were developed to describe this phenomenon. In the fluid picture, Biglari et al. [33] suggested to describe the reduced transport in the pedestal region as a consequence of a poloidal $\mathbf{E} \times \mathbf{B}$ shear of the plasma flow caused by the radially changing electric field E_r. Due to this shear the spatial correlation length of turbulences is lowered which results in a decrease of diffusion.

Viezzer et al. showed in [34] the neoclassical nature of the radial electric field in the pedestal region. In this region the radial electric field was found to behave like

$$E_r \approx \frac{\nabla p_i}{e n_i} \tag{6.1}$$

In a fully developed pedestal the gradient ∇p_i is responsible for the improved confinement. E_r reaches values around -60 kVm^{-1} in the pedestal region where anywhere else it is greater than zero. Generally, it is hard to detect this strong field gradient experimentally because high spatial resolution of the diagnostics is required and was only achieved in latest investigations [35].

The collapse of the pedestal due to the ELM flattens the ion pressure profile $p_i = n_i T_i$ and therefore reduces the gradient ∇p_i which leads further to a reduction of the poloidal flow shear caused by E_r. Thereby the decorrelation of turbulences is reduced and higher radial transport is expected. After the ELM

the pressure profile p_i recovers and the poloidal shear develops again. Due to the accompanied decreasing correlation length of turbulences the transport continuously reduces.

If a constant neutral source is included into the simulations, D decreases from a relatively high value after the ELM to pre-ELM level with a decay-like characteristic. Because of the constant plasma fueling by neutrals a higher diffusion coefficient is observed. During the recovery of the shear flow transport is continuously reducing. This is exactly the case observed in phase I for calculations with a constant particle source. Considerations like these give a possible explanation for the increased diffusion coefficient in phase I.

Phase I is also called the *quiet* phase due to its missing magnetic signature. In this phase the ion saturation current in the divertor is observed to be low. The particle flux $\mathbf{\Gamma}$ is approximated by Fick's law

$$\mathbf{\Gamma} = -D\nabla n \qquad (6.2)$$

Interpreting the results for D in phase I one can conclude that the reduced particle flux is caused by the small density gradient ∇n in phase I.

In phase II no clear statement is possible. The higher particle flux in the divertor could be due to the steep gradients only, but also because of an increased D additionally. The mid-frequency signature, which determines phase II, could be related to an increased D or not. The increasing ∇T_e leads to a higher heat flux into the SOL, changing the pressure balance in the divertor towards lower n_e.

The appearance of high frequency fluctuations in phase III either does not change D, or even reduces D when compared to phase II.

In summary, no clear impact of the different magnetic modes, which are clearly visible in the magnetic signals and which can be correlated with the recovery behavior of n_e and T_e profiles, on the interpretatively determined particle diffusion coefficient can be seen. This might lead to the conclusion that MHD modes, visible in the magnetics, are not the modes which dominate particle transport.

6.3. Outlook

In this thesis the diffusion coefficient D was calculated including different particle sources in the pedestal. A possible explanation of the behavior of D was sketched but further investigations are necessary to underline the given hints in the previous section.

In this work only the confined region of the plasma was considered and physics in the scrape-off layer were roughly estimated. To obtain more reliable results the transport model needs to be improved. Because of the uncertainty coming from the neutrals, calculations with the SOLPS (Scrape-off layer physics) code package are suggested to estimate their behavior outside the confined plasma.

The changing equilibrium during the ELM crash was not taken into account in this work. This could cause effects not considered here especially after the ELM during its recovery. However, quick tests showed these effects to be generally small compared to the effect of incoming neutrals, but should be taken into account for accurate simulations.

Another improvement of the model would be the consideration of the neutral beam injection. Although the beam neutrals are highly energetic and focused to fuel and heat the core of the plasma it cannot be excluded that some particles get ionized in the pedestal and act as a plasma source as well.

Simultaneous modeling of n_e, T_e and T_i could be performed to see, whether the stagnation of the recovery of T_e in phase I is due to increased heat transport or because of the rising number of particles.

Long term goal is to quantify the diffusion coefficient taking incoming neutrals into account. The general dependence on the neutral energy and density could be shown in this work. Next possible steps could be the quantification and characterization of the neutral source including processes in the scrape-off layer. Also the consideration of different neutral species with different velocity distributions is open for future investigations. In general this would help to give deeper insights into the transport mechanism in a tokamak plasma and add another piece to the puzzle of a controlled nuclear fusion reactor.

A. Acknowledgement

Da es üblich ist an dieser Stelle der Diplomarbeit seinen Dank an die Personen zu richten, die maßgeblich zu dem Erfolg der Arbeit beteigetragen haben, möchte auch ich diese schöne Tradition fortsetzen und die Gelegenheit nutzen ein paar persönliche Worte zu verfassen.

Ein großer Dank richtet sich an *Friedrich Aumayr* von der TU-Wien, der aufgrund seiner Kontakte ermöglicht hat, diese Arbeit an einem externen Instiut ohne Schwierigkeiten durchzuführen. Auch wenn die Besuche in Wien sich während der Arbeit in Grenzen hielten, habe ich immer einen Platz in seinem Institut gefunden.

Ohne Zweifel kann man sich keine bessere Betreuung als die von *Elisabeth Wolfrum* vorstellen. Die Arbeit am IPP hat eine unglaubliche Freude bereitet und war andauernd motivierend. Dazu haben ihre Geduld und Bereitschaft, Dinge auch öfters zu erklären einen wesentlichen Beitrag geleistet.

Eine wichtige Rolle im Zuge dieser Arbeit wurde von *Florian Laggner* eingenommen. Als direkte Ansprechperson in Wien und mit seiner für ihn selbstverständlichen Hilfsbereitschaft hat er viel zum Gelingen dieser Arbeit beigetragen.

Den Einstieg in den ASTRA Code hat mir *Emiliano Fable* sehr erleichtert. Er war auch stets zur Stelle, wenn es Unklarheiten bei den Simulationen gab.

Ein großer Dank sei auch an meine Kollegen und Freunde, die ich in Garching kennen gelernt habe, gerichtet, mit denen es immer bunte Abwechslung gab. Dabei denke ich besonders an *Javier*, *Emile* und *Anton*. Auch *Jakob*, der schon früher nach Wien zurück gekehrt ist, und *Sergiu* seien hier erwähnt. Sportliche Aktivitäten und auch nächtliche Touren durch München haben nicht gefehlt.

An *Klara*, *Marvin* und *Siri* sollen auch noch ein paar Gedanken gerichtet werden. Vielen Dank für die lustigen Zeiten in Bremen und auch immer wieder beim Mittagessen in der Kantine. Mein Freund *Ahmed*, sowie die Doktoranden und wissenschaftlichen Mitarbeiter *Nils*, *Felician*, *Gregor* dürfen an dieser Stelle nicht fehlen.

Ein weiterer Doktorand, *Georg*, sei besonders hervorgehoben, der mir in der letzten Phase der Arbeit den nötigen Motivationsboost zum Durchhalten gegeben hat.

Den Kollegen von der Arbeitsgruppe in Wien möchte ich einen herzlichen Dank aussprechen, auch wenn ich sie leider nur selten gesehen habe. Die Konversationen im Gruppen-Chat sind immer sehr unterhaltsam.

Die übrigen zwei Mitgliedern des *Physiker Quaddro*, *Bene* und *Coco*, neben dem bereits erwähnten *Georg*, dürfen nicht vernachlässigt werden. Das Studium wäre ohne ihre Freundschaft wohl nur 1/7 so lustig gewesen. Danke für die Unzahl erheiternder Geschichten, die dabei entstanden sind.

Meine Freunde in Wien sollen an dieser Stelle gegrüßt werden: *Schöberl, Winkler, Corrado, Paul, Martin, Domi, Rainer, Gratzer, Alex*. Meine Musiklehrer *Dieter* und *Andreas* sowie meine Musikfreunde *Bastiaan, Konsti, Kevin, Max, Lilli, Christof* und *Matthias* ebenfalls.

Das Wichtigste kommt bekanntlich zum Schluss und den habe ich für meine Eltern *Maria* und *Harald*, sowie meine Geschwister *Therese, Bernadette* und *Matthias* reserviert. Man kann es nicht stark genug betonen, dass ich ohne den soliden Rückhalt meiner ganzen Familie nie so dorthin gekommen wäre, wo ich jetzt bin.

Eine wichtige Person fehlt noch um den Kreis zu schließen. Danke, *Stefanie*, für deine Liebe, Geduld und Vertrauen. Ihre Heiterkeit ist stets ungebrochen und zählt zu den wichtigsten Komponenten in meinem Leben.

Bibliography

[1] D. Ganser, *Europa im Erdölrausch*, Orell Füssli Verlag AG, Zürich 2012

[2] J. P. Freidberg, *Plasma Physics and Fusion Energy*, Cambridge University Press, New York 2007

[3] J. Wesson, *Tokamaks*, Clarendon Press, Oxford 2004

[4] U. Stroth, *Plasmaphysik*, Vieweg+Teubner Verlag, Wiesbaden 2011

[5] A. Fasoli, *Nuclear Fusion and Plasma Physics*, Lecture Notes, École Polytechnique Fédérale de Lausanne, 2015

[6] N. J. Peacock, D. C. Robinson, M. J. Forrest, et al., *Measurement of the Electron Temperature by Thomson Scattering in Tokamak T3*, Nature **224** (1969) 488-490

[7] A. O. Burckhart, *Different ELM regimes at ASDEX Upgrade and their linear stability analyzis*, PhD thesis, Ludwig Maximilian Universität, München 2013

[8] F. Wagner, G. Becker, K. Behringer, et al, *Regime of Improved Confinement and High Beta in Neutral-Beam-Heated Divertor Discharges of the ASDEX Tokamak*, Phys. Rev. Lett. **49** (1982) 1408

[9] K. Miyamoto *Plasma Physics and Controlled Nuclear Fusion*, Springer-Verlag Berlin Heidelberg, Berlin 2005

[10] F. Wagner, *A quarter-century of H-mode studies*, Plasma Phys. Control. Fusion **49** (2007) B1-B33

[11] J. W. Connor, *A review of models for ELMs*, Plasma Phys. Control. Fusion **40** (1998) 191

[12] F. M. Laggner, *Inter-ELM pedestal structure in ASDEX Upgrade*, PhD thesis, Technische Universität Wien, Wien 2017

[13] S. Keerl, *Divertor and pedestal dynamics in between edge localized modes at ASDEX Upgrade*, master's thesis, Technische Universität Wien, Wien 2016

[14] A. Burckhart, E. Wolfrum, R. Fischer, et al., *Inter-ELM behaviour of the electron density and temperature pedestal in ASDEX Upgrade*, Plasma Phys. Control. Fusion **52** (2010) 105010

[15] T. E. Sharp, *Potential-energy curves for molecular hydrogen and its ions*, Atomic Data **2** (1971) 119-169

[16] H. J. Sun, E. Wolfrum, T. Eich, et al., *Study of near scrape-off layer (SOL) temperature and density gradient lengths with Thomson scattering*, Plasma Phys. Control Fusion **57** (2015) 125011

[17] M. Willensdorfer, E. Fable, E. Wolfrum, et al., *Particle transport analysis of the density build-up after the L-H transition in ASDEX Upgrade*, Nucl. Fusion **53** (2013) 093020

[18] A. V. Chankin, D. P. Coster, R. Dux, et. al., *SOLPS modelling of ASDEX upgrade H-mode plasma*, Plasma Phys. Control. Fusion **48** (2006) 839-868

[19] R. Dux, *Plasmaphysik und Fusionsforschung Teil II: Fusionsforschung*, Lecture Notes, Universität Augsburg, 2002

[20] T. Lunt, F. Reimold, E. Wolfrum, et al., *Influence of the first wall material on the particle fuelling in ASDEX Upgrade*, Plasma Phys. Control. Fusion (accepted)

[21] R. Fischer, C. J. Fuchs, B. Kurzan, et al., *Integrated data analysis of profile diagnostics at ASDEX Upgrade*, Fusion Science and Technology **58** (2010) 675-684

[22] M. Willensdorfer, *Fast chopping of a lithium beam for plasma edge diagnostic at ASDEX Upgrade*, master's thesis, Technische Universität Wien, Wien 2009

[23] W. Suttrop, *Electron Cyclotron Emission Plasma Diagnostics*, IPP Report 1/306

[24] F. M. Laggner, S. Keerl, E. Wolfrum *Divertor, scrape off layer and pedestal particle transport dynamics in the ELM cycle on ASDEX Upgrade*, Plasma Phys. Control. Fusion, in preparation 2017

[25] G. V. Pereverzev, *ASTRA - Automated System for TRansport Analysis*, IPP Reports 5/98, 2002

[26] F. L. Hinton and R. D. Hazeltine *Theory of plasma transport in toroidal confinement systems*, Reviews of Modern Physics, **48** (2), Part I (1976) 239-308

[27] B. LaBombard, *KN1D: A 1-D Space, 2-D Velocity, Kinetic Transport Algorithm for Atomic and Molecular Hydrogen in an Ionizing Plasma*, Plasma Science and Fusion Center, Massachusetts Institute of Technology, Cambridge USA, 2001

[28] M. Wischmeier, A. Kallenbach, A. V. Chankin, et al., *High recycling outer divertor regimes after type-I ELMs at high density in ASDEX Upgrade*, Journal of Nuclear Materials **363-365** (2007) 448-452

[29] S. Brezinsek, S. Wiesen, D. Hartig, et al., *Characterisation of the deuterium recycling at the W divertor target plates in JET during steady-state plasma conditions and ELMs*, Phys. Scr. **T167** (2016) 014076

[30] M. Dunne, Intern Discussion, 27th February 2017

[31] J. D. Callen, R. J. Groebner, T. H. Osborne, et al., *Analysis of pedestal plasma transport*, Nucl. Fusion **50** (2010) 064004

[33] H. Biglari, P. H. Diamond, P. W. Terry *Influence of sheared poloidal rotation on edge turbulence*, Phys. Fluids B **2** (1), (1990)

[34] E. Viezzer, T. Pütterich, C. Angioni, et al., *Evidence for the neoclassical nature of the radial electric field in the edge transport barrier of ASDEX Upgrade*, Nucl. Fusion **54** (2013) 012003

[35] M. Cavedon, T. Pütterich, E. Viezzer, et al., *Pedestal and E_r profile evolution during an edge localized mode cycle at ASDEX Upgrade*, Plasma Phys. Control. Fusion, submitted 2017